Thermo-aqueous coupling behaviors for shape memory hydrogels: A statistical–mechanical model and simulations faced with experiments

Yunqiang Hu [a], Chengjun Zeng [a], Martine Ben Amar [b], Fei Jia [a,*], Yanju Liu [a], Jinsong Leng [c,*]

[a] *Department of Astronautical Science and Mechanics, Harbin Institute of Technology (HIT), P.O. Box 301, No. 92 West Dazhi Street, Harbin 150001, People's Republic of China*
[b] *Laboratoire de Physique de l'Ecole normale supérieure, ENS, Université PSL, CNRS, Sorbonne Université, 24 rue Lhomond, 75005 Paris, France*
[c] *Center for Composite Materials and Structures, Science Park of Harbin Institute of Technology (HIT), P.O. Box 3011, No. 2 YiKuang Street, Harbin 150080, People's Republic of China*

ARTICLE INFO

ABSTRACT

The shape memory behavior of hydrogels endows themselves with the capacities of shape programming and shape recovering, which have great potential in many fields, such as drug release and soft robotics. In thermally responsive hydrogel, particularly, there are two critical factors, temperature and water, that can induce the shape memory effect(SME). Temperature-induced SME has been extensively studied, while water-induced SME has been rarely investigated. In our work, the combined effect of water and temperature on shape memory behavior of hydrogels is experimentally studied and deeply analyzed from a physical perspective. We found that the shape fixed ratio of shape memory hydrogels (SMHs) increases monotonically with temperature, but first increases and then decreases with water content. Moreover, it exits a nonlinear coupling between the water and temperature effects on the SME. On the basis of these findings, a constitutive model is developed to capture this thermo-aqueous coupling using the statistical theory of transient networks, from which we obtain an explicit evolution equation of deformation gradient. In the proposed theory, the temperature-induced SME is investigated through the temperature-water responsive association and dissociation of dynamic bonds while the water-induced SME is explained by the variation of the glass transition temperature according to the Fox–Flory model. Finally, and to provide a final test of the theoretical work, it is implemented into a user element (UEL) subroutine which provide simulations in agreement with our experiments. Our work is expected to provide guidance for future application of SMHs.

1. Introduction

Shape memory hydrogels (SMHs) were first reported by Osada and Matsuda (1995), and a variety of stimulus-responsive (e.g., temperature, PH, magnetic, and salt) SMHs have been rapidly fabricated in recent years (Luo et al., 2015; Maiti et al., 2020). Shape memory effect (SME) of SMHs describes the ability of SMHs to be programmed and to recover their initial shape under stimuli (Zhang et al., 2018; Lówenberg et al., 2020). Compared with shape memory materials made of polymer/inorganic composites and carbon-based materials, SMHs have attracted great attention due to their softness, excellent biocompatibility, and have been used in drug delivery, bioengineering and soft robotics (Techawanitchai et al., 2012; Shang et al., 2019).

Despite the practical importance of SMHs in our daily lives and their implication in many industrial processes, there is no real modeling for these materials when they are sensitive to both temperature and water content variations. Indeed, if in the last years, great progress have been

achieved in the elaboration of thermally sensitive SMHs and in the understanding of the dynamics of networks and polymer chains, much less studies concern water responsive gels, in the same framework, the coupling of water and temperature shape memory properties. Then we aim to elaborate a complete analysis of shape memory hydrogels responsive both for water and temperature variations which will be confronted to simulations and experiments. A new temperature-water coupling method is provided to fabricate complex shapes for microdevices of sensors, actuators and biomedical components. Constructing two networks is one of the common method achieving thermally responsive SMHs (Chen et al., 2020; Dai et al., 2019): one is a permanent network that is loose and insensitive to external stimuli, and the other one is a transient network. At the network level, the shape memory effect can be understood through the dynamic cross-linking and the chain mobility. The dynamic cross-linking can be affected by breaking/reforming of dynamic bonds, e.g. hydrogen bond, hydrophobic

* Corresponding authors.
  E-mail addresses: feijia@hit.edu.cn (F. Jia), lengjs@hit.edu.cn (J. Leng).

interaction and dynamic covalent bond (Lu et al., 2017; Perera and Ayres, 2020), attached to the transient network. Responsive units in the molecular chain can be activated and deactivated under external stimuli, especially temperature for thermally responsive SMHs. Heat alters the energy barrier required to form the transient network by free chains. Consequently, deformed shape can be recorded and recovered by the transient network, this process being defined as temperature-induced shape memory (T-SME). For instance, Hu et al. (2018) reported a double network SMH through hydrophobic interaction of Methyl-cellulose. At low temperature, water molecules form clathrates and chains are not cross-linked. After heating, chains are cross-linked due to aggregation of the hydrophobic groups. By forming robust hydrogen bonds between two networks, Xu et al. (2018) developed a tough SMHs. The shape memory effect caused by the chain mobility can be named as water-induced shape memory (W-SME) as mentioned in Zhang et al. (2014), because chain mobility is mainly dependent on the water content through SMHs swelling and drying process. Zhao et al. (2019) experimentally studied W-SME of nano-composite hydro-gel and showed that programmed shape can be fixed by drying or recovered by swelling. The fact that the water content also affects the dynamic cross-linking (Annable et al., 1996; Chen et al., 2009), demonstrates the existence of an interaction between the two shape memory effects.

To illustrate this interaction between W-SME and T-SME, a demon-stration experiment shown in Fig. 1 was conducted. A rectangular plate made of swollen SMHs was initially twisted into a helical shape at low temperature. Rising the temperature, SMHs can maintain the deformed shape without any constraints. Drying out SMHs and then lowering the temperature, the helical shape was maintained rather than recovering its initial shape. These results suggest that T-SME is significantly affected by moisture and the role of T-SME and of W-SME are coupled. The shape recovery can only be observed after water absorption. This thermo-aqueous coupling shape memory behavior is imperative for applications in SMHs. However, the coupling behavior is less studied and most of existing studies considered these two type of SMEs separately.

For T-SME, the shape memory model has to involve different molec-ular chains with various reference configurations. To accommodate this feature, Long et al. (2010) presented a 1D theoretical frame-work for soft active materials. This model was extended to the 3D case (Ge et al., 2012, 2014) and was also used by Mao et al. (2019), in which plasticization was considered. These models were built through a macroscopic approach and the evolution equation of the deformation gradient was implicit. Apart from this approach, another effective way to model polymeric materials is a micro-macro modeling approach based on chain statistic theory. Due to the clear physical meaning and accuracy in capturing material properties, this approach was in-troduced in hyperelastic (Wall and Flory, 1951), viscoelastic (Vernerey et al., 2017) and viscoplastic (Mahjoubi et al., 2019) material mod-elings. Moreover, micro-macro modeling approach is a powerful way to obtain an explicit evolution equation of deformation gradient for T-SME.

The mechanism of hydrogels W-SME is the variation of the mobility of chain caused by the polymer volume fraction ϕ, which leads to the variation of two parameters, elastic modulus E and the glass transition temperature T_g from macroscopic view. Following Flory-Rehner theory, E was of order $\phi^{1/3}$, but experimental observations showed that E is of order $\phi^{0.56}$ and $\phi^{2.3}$ for swelling and dehydration processes, respectively (Li et al., 2020). Although some works have investigated the $\phi-T_g$ relationship of polymers (Xiao and Nguyen, 2013; Mao et al., 2019), the applicability of these results to hydrogel materials with a large number of water molecules still needs to be confirmed.

The models discussed above regarding shape memory effects con-cern polymers with no or low moisture. Though there are copious works for hydrogels (Hong et al., 2008; Chester et al., 2015; Curatolo et al., 2022; Ben Amar et al., 2011; Curatolo et al., 2021; Lin et al., 2020; Ge et al., 2021; Qu, 2022; Li et al., 2021), there is a scarcity of models for shape memory hydrogels. For SMHs, a constitutive model was recently established by Chen et al. (2021). In addition, reversible shape memory behaviors of N-isopropylacrylamide based SMHs was also studied in a previous work (Hu et al., 2022) by our team. How-ever, these two models were based on macroscopic methods and the evolution equation of the deformation gradient for temporary network was imperfect. More importantly, these models do not incorporate the combined thermo-aqueous shape memory. In this work, a constitutive model is established through the transient network theory to capture the key features of thermally-induced double network SMHs. We in-vestigate several dynamic features occurring at the microscopic scale such as: the thermo-aqueous responsive association and dissociation of dynamic bonds, the water associated aggregation strength and the maximum value of water-associated polymerizable molecular chains per unit volume. For the bond association/dissociation, we choose the temperature responsive energy barrier and for the W-SME the Fox–Flory equation (Fox and Flory, 1950).

The organization of this paper is described as follows. Material and experimental methods for water diffusion, isothermal uniaxial tensile testing, and shape memory cycling are presented in Section 2. Section 3 describes the developed constitutive model, the finite element implementation of UEL in ABAQUS software and the procedure for determining the parameters from the experimental results of Section 2. In Section 4, we compare numerical predictions and experimental observations. Section 5 is devoted to the conclusion. Finally, some technical proofs are detailed in the Appendix.

2. Experiments

In order to validate all aspects of our model, we decided to perform our own experiments. This allows a perfect knowledge of all mechanical and thermal constants which will be introduced in the simulations. The material is described below as the different steps of the experimental study.

2.1. Material

The Acrylamide(AAm)-Methylcellulose(MC) cooling-triggered dou-ble network SMH was synthesized according to the protocol established by Hu et al. (2018). All materials were purchased from Aladdin Indus-trial. AAm(18 $wt.\%$) in low concentration of N, N'-methylenebisacrylamide (0.03 mol% relative to AAm) and MC(6 $wt.\%$) were mixed in water (76 $wt.\%$), in addition with a photoinitiator: 2-hydroxy-4′-(2-hydroxyethoxy)-2-methylpropiophenone. Then, the polymer solution was exposed to 365 nm of UV light at 10 °C for 6 h to polymerize, thus obtaining the required SMHs.

2.2. Free swelling test

To characterize the water diffusion of SMHs, a set of free swelling tests at different temperatures were performed on cuboids of SMS specimens of size 10 mm × 10 mm × 0.4 mm, at different temperatures: 283 K, 313 K and 343 K. Notice that because a certain quantity of water remains in the specimens obtained by the previous method, they need to be dried before any measurement. After drying, the water content was 15% and initial mass of SMHs m_0 was recorded. Then, the specimens were completely immersed in water for some time denoted by t_m and taken out to measure their current mass $m(t_m)$ to evaluate the water mass fraction defined by $\phi_W(t_m) = 1 - 0.85m_0/m(t_m)$. The volume fraction of water, approximately equal to its mass fraction $\phi_W(t_m)$, is shown as a function of t_m, under different temperatures in Fig. 2. It can be observed that the water diffusion which lasts about 1000 s at 283 K becomes very fast at moderate higher temperatures. The equilibrium water concentration decreases only slightly as the temperature increases.
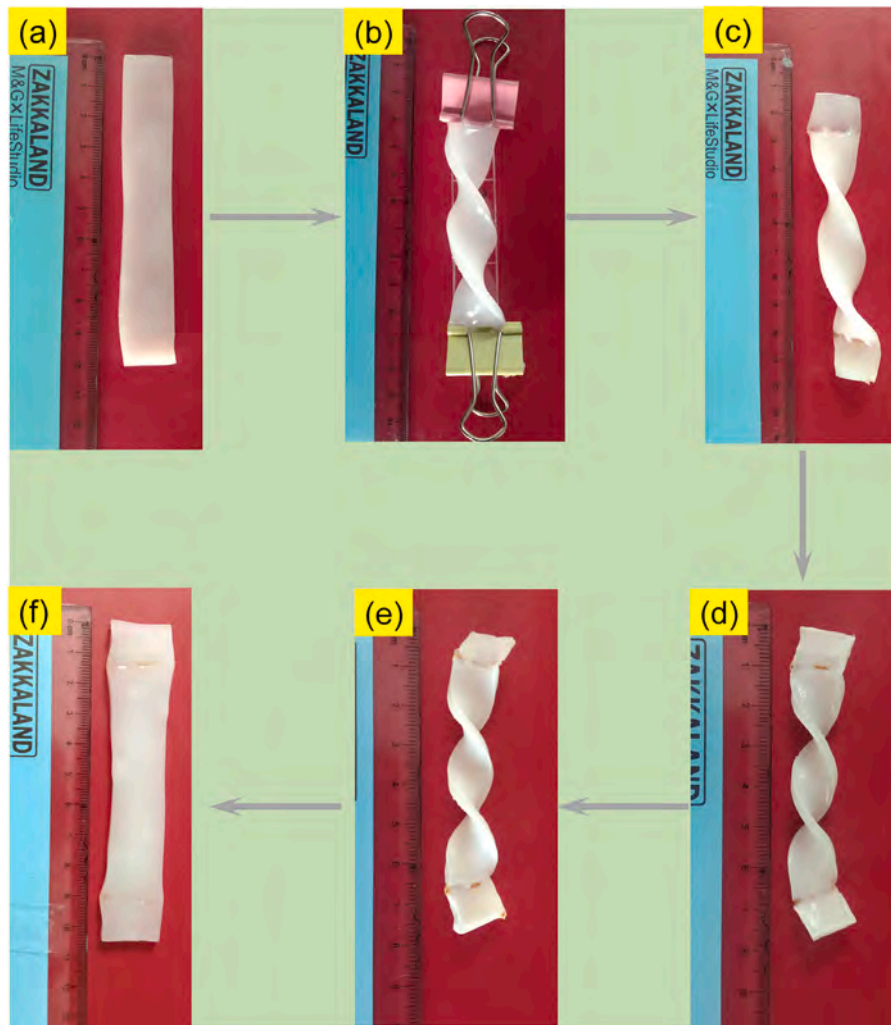
Fig. 1. A demonstration experiment for thermo-aqueous coupling shape memory behavior of a SMH sample: (a) initial shape of SMH strip, (b) deformed SMH at low temperature, (c) heating and suppression of loads, (d) drying at high temperature, (e) cooling, and (f) shape of the SMH sample after swelling.
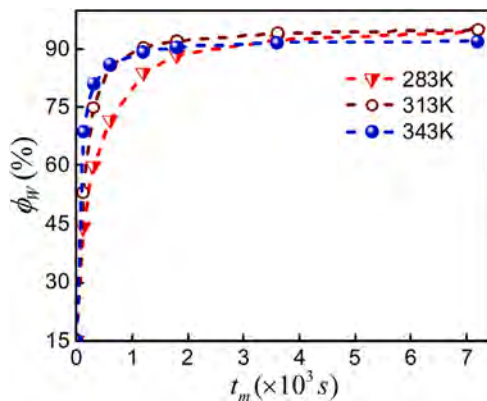

Fig. 2. Water content ϕ_W versus the diffusion time t_m for different imposed temperatures: 283 K, 313 K and 343 K.
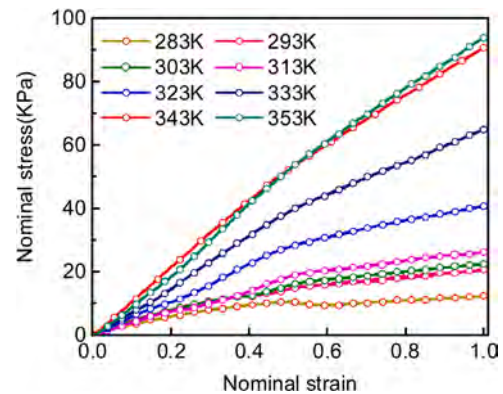

Fig. 3. Nominal stress versus nominal strain obtained by isothermal uniaxial tension test at various temperatures.

2.3. Isothermal uniaxial tension test

A series of isothermal uniaxial tension tests were performed to measure the finite deformation of SMHs under different temperatures varying between 283 K to 353 K. The synthesized SMHs were prepared with stencils and mechanically cut into dogbone shapes with dimensions 18 mm × 4 mm × 3 mm to obtain suitable tensile specimens. All tests were conducted on a tensile machine (SHIMADZU, AGS-X-10KN) at a loading rate of 20 mm/min. To maintain a initial ϕ_W of 76% equivalent to polymer volume fraction ϕ of 0.24 throughout the process, the specimens were soaked in dimethyl silicone oil which
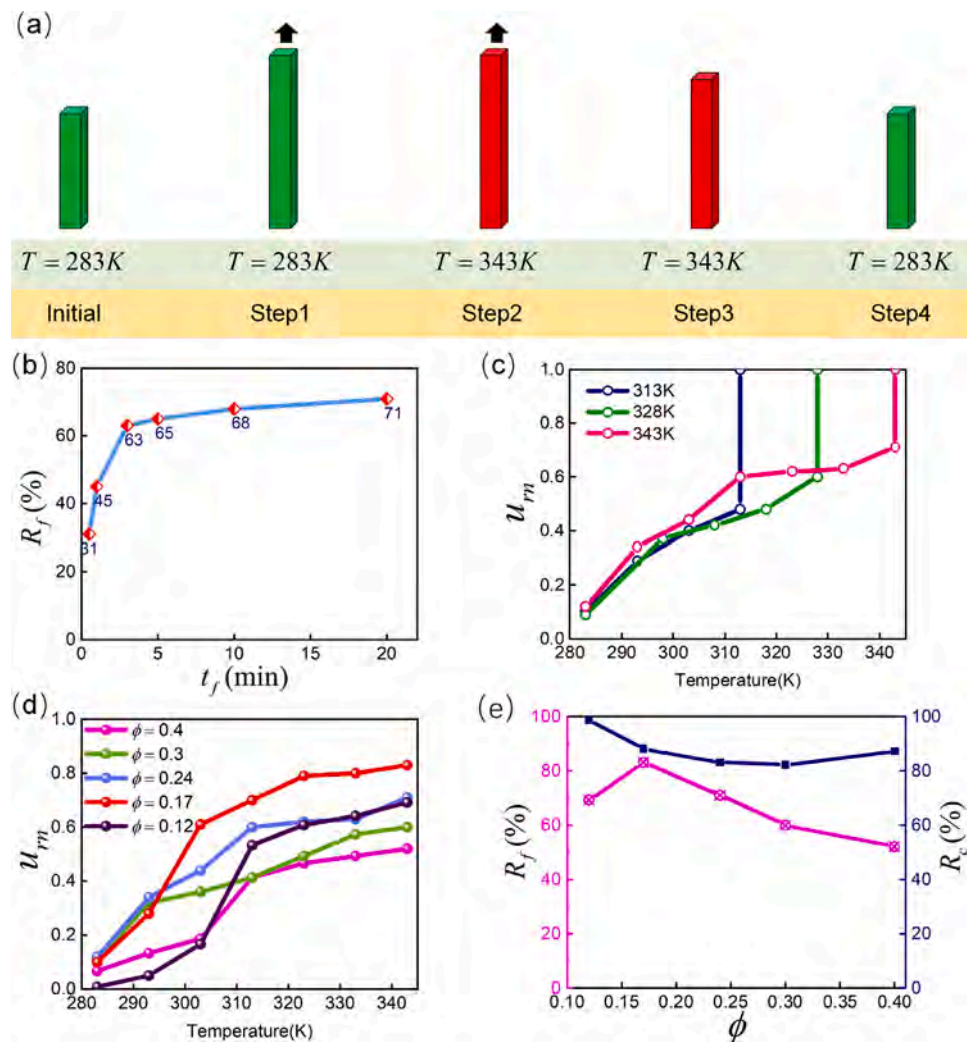
Fig. 4. Isoconcentration shape memory cycle experiments. (a) Schematics of mechanical boundary conditions and temperature set at each step. (b) Curve of shape fixed ratio R_f versus the held fixed time at 343 K with $\phi = 0.24$. (c) Normalized displacement and temperature during removing constraints (Step 3) and free recovery processes (Step 4) at three fixed temperatures (313 K, 328 K and 343 K). (d) Normalized displacement and temperature during Step 4 with different polymer volume fraction (0.12, 0.17, 0.24, 0.3 and 0.4). (e) Shape fixed ratio R_f and shape recovery ratio R_c vs. polymer volume fraction ϕ.

inhibits the evaporation of water. All tests were repeated three times under the same experimental conditions to reduce possible errors and the results shown in Fig. 3 indicate the increase of SMHs stiffness with temperature.

2.4. Shape memory performances

As pointed out in Section 1, the shape memory property of SMHs is related to both temperature and water content. To definitely understand the coupling between each other, we developed two classes of experiment designs. First class will consist in temperature-induced shape memory cycle at different fixed values of the water content, which is a way to decouple the contributions of temperature and water and to realize more intuitive observations on the shape memory performance. The second class consists in changing successively the temperature and the water content in a single shape memory cycle. More experimental details are presented below.

2.4.1. Isoconcentration shape memory cycle experiments

To focus on thermo-mechanical properties of SMHs, experiments were conducted on a cuboid with size: 20 mm × 15 mm × 3 mm at different polymer volume fraction including 0.4, 0.3, 0.17 and 0.12. The specimens having initially a 76% water content were dried or

immersed in water to reach the desired value of water concentration. Herein, the conventional four-step shape memory cycle experiment was adopted (Qi et al., 2008), as shown in Fig. 4(a). (Step 1) First, the specimen was stretched to 150% of its original length L_0. (Step 2) Second, it was heated to 343 K by means of an silicone oil bath, which maintained a constant water content, at fixed displacement loading lasted for a certain time called the held fixed time t_f. In Step 3, the loading was suppressed and its stationary length was recorded as L_f. (Step 4) Finally, the temperature of the specimens was decreased from 343 K to 283 K in the silicone oil bath, and the specimen length at 283 K was recorded as L_c.

Shape memory performance is mainly characterized by two parameters: the shape fixed ratio and the shape recovery ratio, defined as $R_f = L_f/L_0$, and $R_c = 1 - L_c/L_f$, respectively. The experimental results about R_f is presented in Fig. 4(b), as a function of the held fixed time t_f for a specimen of $\phi = 0.24$ at 343 K. One can notice that R_f increases drastically with the time t_f until a critical value, beyond which R_f slowly increases with respect to t_f. Therefore, the held fixed time is chosen as 30 min in later experiments to ensure the experimental reproducibility. Fig. 4(c) shows the variation of the normalized displacement u_{rn} (The ratio of the displacement at the one side of specimen to the amount of stretching at this end of the Step 1.) of the stretched specimen ($\phi = 0.24$) with the temperature for
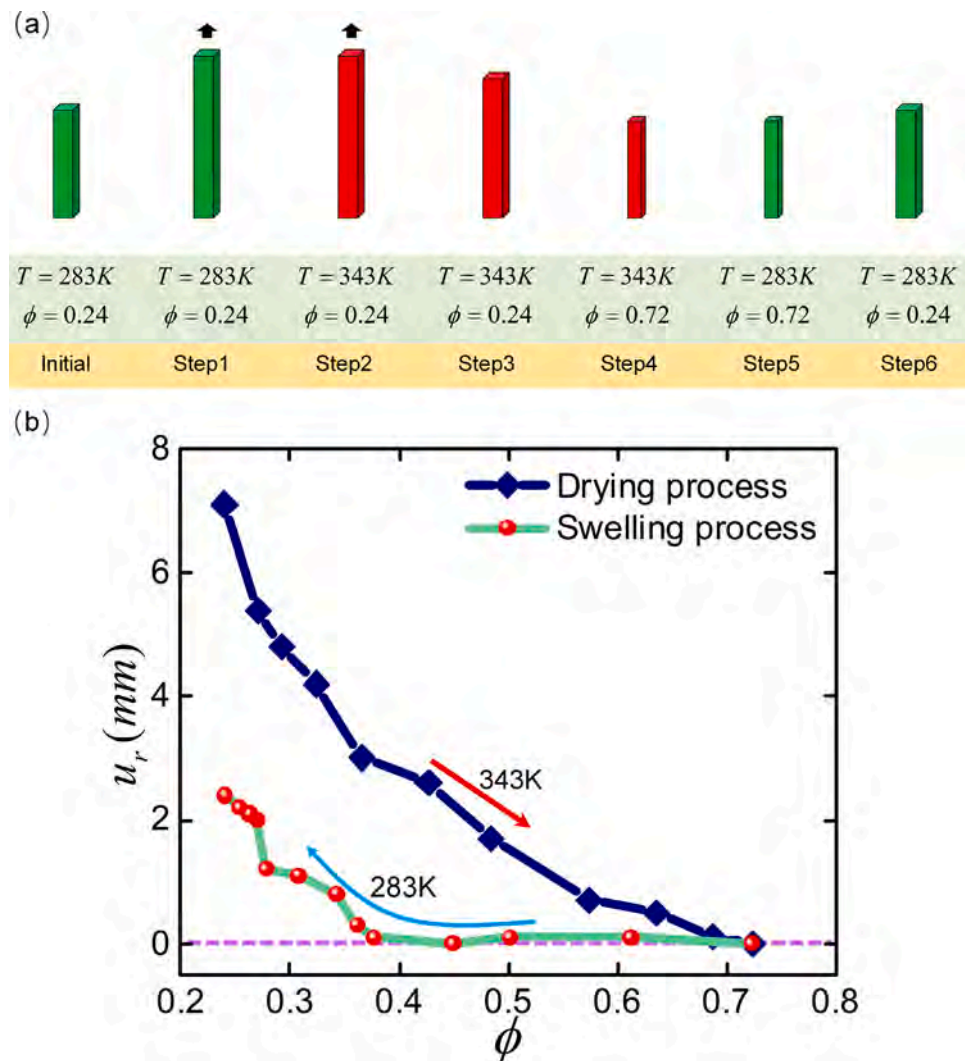
Fig. 5. (a) Schematics of mechanical boundary conditions, temperature and polymer volume fraction set at each step. (b) Displacement of one end of the strip versus polymer volume fraction during drying process at 343 K and swelling process at 283 K.

different fixed temperature values in the shape free recovery process, which demonstrates that R_f increases monotonically with the values of the fixed temperature. Fig. 4(d) depicts the relationship of u_{rn} and temperature of the stretched specimen with different ϕ for the same shape fixed temperature 343 K in the shape free recovery process. The radii R_f and R_c varying with ϕ are presented in Fig. 4(e). It can be seen that ϕ has only a slight effect on R_c, and R_f indicating first an increase and then a decrease as ϕ increases.

2.4.2. Thermo-aqueous coupling shape memory behavior

To investigate the underlying mechanism of the shape memory behavior shown in Fig. 1, a series of thermo-aqueous cycle experiments were performed, with the protocol described in Fig. 5(a). (Step 1) Firstly, a cuboid specimen ($\phi = 0.24$) of 20 mm × 15 mm × 3 mm was stretched with a 10 mm length increase at 283 K. (Step 2) Secondly, the temperature of the stretched specimen was raised to 343 K by means of an oil bath keeping the loading condition. (Step 3) Thirdly, the load was removed and the specimen exhibited a temporary shape, retaining most of the given deformation. (Step 4) Fourthly, the same specimen was transferred to an oven with 343 K to reduce its water content and the length of the specimen were recorded at regular intervals. (Step 5) Then, the temperature of the specimen was lowered to 283 K by means of an oil bath, which ensures that its temperature decreased but the water content was kept constant. (Step 6) Finally, the specimen was

immersed in water at 283 K to increase the water concentration, during which the polymer volume fraction and the length of the specimen were recorded at regular time intervals. Since the deformation of soft cuboids is simple, their thermo-aqueous shape memory performance can be directly obtained by the specimen length. The variation of one end displacement u_r varying with ϕ from drying (Step 4) to free swelling (Step 6) was shown in Fig. 5(b). Compared to conventional shape memory cycle, it is different that there was almost no shape recovery during cooling in Step 5, which may result from the fact that the transition temperature of SMH specimens increased as ϕ increased.

Noticing that if SMHs were shortened to their initial length at the end of step 4, the specimen length could be kept, while the deformation only occurred in the other two directions at the beginning of free swelling (Step 6) and the length of specimen increased as ϕ further decreased.

3. Constitutive model

Based on the experimental observations given in Section 2, we establish a theoretical model to capture the thermo-aqueous shape memory behaviors of double network SMHs. Indeed, we imagine that two networks are juxtaposed: a permanent and a temporary one as shown in Fig. 6(a). The permanent network looks like a conventional hydrogel network. Water content can modify the chain mobility (Mao
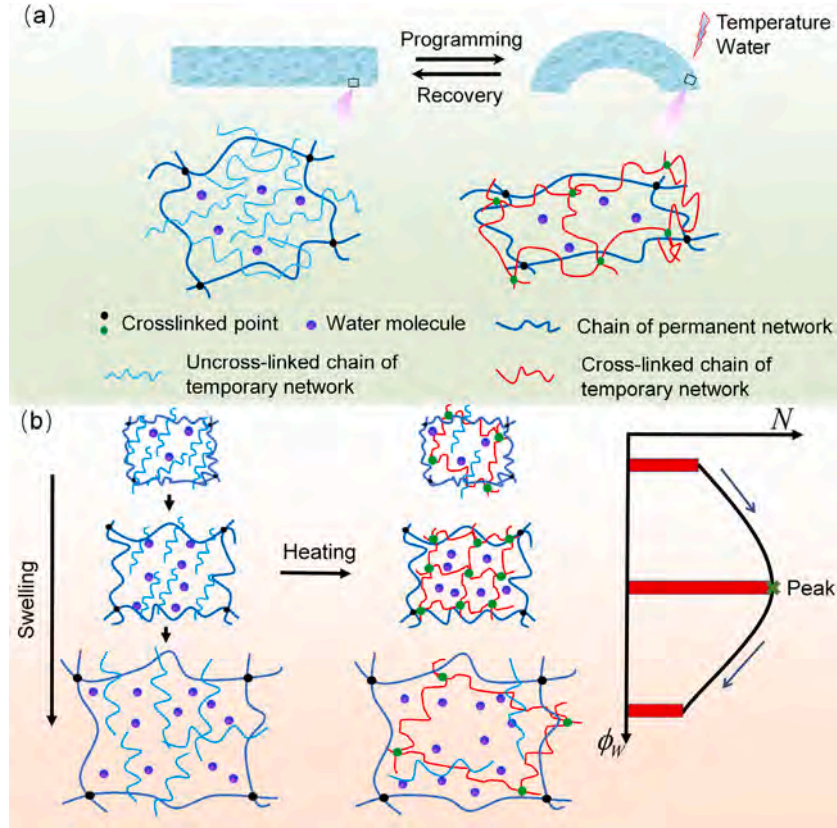
Fig. 6. (a) Representation of the shape memory process for double network SMHs. At low temperature, chains of the temporary network are in a free state. When SMHs are deformed and heated, the chains in free state are cross-linked to form a temporary network with a fixed shape (shape programming). Then, when cooled the cross-linked chains returns a free state again and SMHs recover their original shape recovery. (b) Effects of temperature and water on both permanent and temporary networks. The permanent network is insensitive to temperature, while its chain mobility decreases with water content. For temporary network, the cross-linked chain number mainly depends on temperature, that is, the higher the temperature, the greater is the cross-linked chain number. In addition, water content also can affect the temporary network cross-linked behaviors through the strength of the dynamic bonds and the density of cross-linkable molecular chains, that is, the cross-linked chain number N first increases and then decreases as water content.

et al., 2019) to induce W-SME, a process known to be captured by the Fox–Flory equation (Fox and Flory, 1950). For the transient network, cross-linking points appear and disappear under specific water content and temperature conditions, as illustrated in Fig. 6(b). This dynamics is controlled by the strength of the dynamic bonds and the cross-linkable molecular chain density. Temperature-water responsive mechanisms for the dynamic bonds will be explained by a statistical thermodynamic approach, by aggregation process induced by water, and by the existence of an upper threshold for the water-associated polymerizable molecular chains per unit volume.

The free energy density of SHMs can be written as (Hong et al., 2008)

$$\Psi(\mathbf{F}, c, T) = \Psi_P(\mathbf{F}, c, T) + \Psi_T(\mathbf{F}, c, T) + \Psi_M(c, T) + U(J, c), \quad (1)$$

where $\mathbf{F}$ is the deformation gradient, c is the mole number of water molecules per reference volume and T is the absolute temperature while $J = \det(\mathbf{F})$ represents the relative volume variation. Ψ_T and Ψ_P denote the free energy of the temporary and permanent networks, respectively. Ψ_M represents the mixing energy and $U(J, c)$ is a penalty term for volume increase. The form of Ψ_M is obtained as (Huggins, 1941; Chester et al., 2015)

$$\Psi_M = \mu_0 c + RT \left[c \ln \frac{\Omega c}{1 + \Omega c} + \frac{\chi c}{1 + \Omega c} \right], \quad (2)$$

where μ_0 is the chemical potential of pure water, χ the Flory–Huggins interaction parameter, Ω the water volume per mole and R the universal gas constant. The incompressible constraint for both networks and solvents used in Hong et al. (2008) is approximated by a quadratic expansion, namely (Bouklas et al., 2015),

$$U(J, c) = \frac{1}{2} K(J - 1 - \Omega c)^2, \quad (3)$$

where K represents the bulk modulus which is far greater than the initial shear modulus.

3.1. Free energy of temporary network

A micro-macro modeling approach (Wall and Flory, 1951; Mahjoubi et al., 2019) is adopted to determine the free energy of temporary networks. Compared with the macroscopic method, this method not only has a clearer physical meaning but also yields an explicit evolution equation of the deformation gradient of the temporary network, which is more convenient for finite element implementations. It is assumed that all the chains initially evenly distribute on the surface of a sphere. Therefore, the free energy density in the current configuration Ψ_T^c can be expressed as (Xiao et al., 2021)

$$\Psi_T^c = \frac{1}{\varpi} \int_0^{2\pi} \int_0^{\pi} N(c, T) \psi \, dS, \quad (4)$$

where ϖ is the area of the unit sphere, $N(c, T)$ the number of cross-linked molecular chains per current volume, dS the elementary solid angle and ψ the energy of single molecular chain. According to the statistical physical modeling of polymers, $\psi = -k_b T \ln p$, where p denotes the probability density function and k_b represents the Boltzmann's constant. For simplicity, for a quantity $\mathcal{A}(\theta, \omega)$ which depends on two angles $0 < \theta \leq \pi$ and $0 < \omega \leq 2\pi$, we will use the notation $\langle \mathcal{A} \rangle$ for $\langle \mathcal{A} \rangle = \frac{1}{\varpi} \int_0^{2\pi} \int_0^{\pi} \mathcal{A} \, dS$, with $dS = \sin \theta \, d\theta \, d\omega$, which means the average of $\mathcal{A}$ over all spatial orientations. In case of possible existence of stresses in the initial configuration, Ψ_T is modified as

$$\Psi_T = J \Psi_T^c = J \left[\langle N \psi(r) \rangle - \langle N \psi(r_0) \rangle \right], \quad (5)$$

where r and r_0 represent the chain lengths in the current and reference configurations, respectively. r_0 can be further written as $r_0 = b\sqrt{M}$ according to the freely-jointed chain model, where b and M denote respectively the Kuhn length and the number of Kuhn segment.

As mentioned previously, the cross-link condition of temporary network varies with temperature and our purpose consists to analyze this variation. We first assume that newly cross-linked chains originated from uncross-linked chains in unbound state are stress-free. The change in temperature is then divided into infinitely tiny steps labeled by i where i goes from 1 to n. During such step, all physical quantities remain constant. Consequently, the average in Eq. (5) can be further expressed as:

$$\langle N\psi(r)\rangle - \langle N\psi(r_0)\rangle = \langle \Delta N_1\psi(r_1) + \Delta N_2\psi(r_2) + \cdots + \Delta N_n\psi(r_n)\rangle$$
$$- \langle N\psi(r_0)\rangle, \tag{6}$$

where ΔN_i and r_i ($i = 1, 2, 3, \ldots, n$) are respectively the number and the length of newly cross-linked chains during the tiny i process. Eq. (6) reflects the fact that different chains have different stress-free configurations. Noting that r_i is related to temperature and deformation history, it is impossible to obtain a simplified formula for Eq. (6) directly. The integral form of free energy for the each newly formed chain is then taken as

$$\langle \psi(r_i)\rangle = \langle\langle p(r, r_i)\psi(r)\rangle\rangle, \quad i = 1, 2, 3, \ldots, n, \tag{7}$$

where $\langle\langle A \rangle\rangle = \int_0^{2\pi}\int_0^{\pi}\int_0^{Mb} A r^2 dr \sin\theta d\theta d\omega$ and the history-related deformation can be expressed by the probability $p(r, r_i)$. The independent variable r_i of ψ is now replaced by r. Substituting Eq. (7) into Eq. (6), we can obtain

$$\langle N\psi(r)\rangle - \langle N\psi(r_0)\rangle$$
$$= \left\langle\left\langle \left[\Delta N_1 p(r, r_1) + \Delta N_2 p(r, r_2) + \cdots + \Delta N_n p(r, r_n)\right]\psi(r)\right\rangle\right\rangle - \langle N\psi(r_0)\rangle. \tag{8}$$

Notice that the deformation of each molecular chain of the temporary network is related to the current deformation, i.e. $r_i = f(r, T_i)$, so $p(r, r_i)$ is replaced by $p(r, T_i)$. In Eq. (8), it can be found that the free energy is not related to summation term. However, N still exists in the form of a summation, which is computationally expensive. Similar to the free energy, N_i is also substituted by N as

$$p(r, T) = \frac{\sum_{i=1}^n \Delta N_i p(r, r_i)}{\sum_{i=1}^n \Delta N_i} = \frac{\sum_{i=1}^n \Delta N_i p(r, T_i)}{\sum_{i=1}^n \Delta N_i} = \frac{\int_{T_0}^T p(r, \Lambda) dN(\Lambda)}{N}. \tag{9}$$

Combining Eqs. (5) and (9), Ψ_T reads

$$\Psi_T(\mathbf{F}, c, T) = J\left[\langle\langle \gamma(r, c, T)\psi(r)\rangle\rangle - \langle N\psi(r_0)\rangle\right], \tag{10}$$

where $\gamma(r, c, T) = N(c, T)p(r, T)$ describes the chain distribution. Different newly formed chains correspond to different reference configurations during their cross-linking. In addition, $N(c, T)$ is related to the water content, see Section 3.4.2. Equivalent relationship can be found in visco-elasticity models with transient networks (Tanaka and Edwards, 1992; Vernerey et al., 2017) and the evolution of $\gamma(r, c, T)$ follows the usual evolution equation:

$$\dot\gamma(r, c, T) + \nabla_r \cdot (\gamma(r, c, T)\dot r) = \zeta(r, c, T) - \xi(r)\gamma(r, c, T). \tag{11}$$

The left hand-side of Eq. (11) represents the material time derivative of γ, involving both the time derivative and the deformation dynamics. The right hand-side of Eq. (11) captures the bond association and dissociation. Since newly cross-linked chains are in a stress-free state, $\zeta(r, c, T)$ is defined as

$$\zeta(r, c, T) = k_a\left(N^t - N(c, T)\right)p_0(r), \tag{12}$$

where k_a is the chain association kinetic rate, N^t is the current number of molecular chains that can be cross-linked, and $p_0(r)$ is a temperature-independent probability density function. Based on a Gaussian statistics (Mistry and Govindjee, 2014), it comes:

$$p_0(r) = \left(\frac{3}{2\pi M b^2}\right)^{\frac{3}{2}} \exp\left(-\frac{3r^2}{2Mb^2}\right). \tag{13}$$

In addition, we assume that dissociation behaviors of bonds formed in different configurations are not affected by the force of the chain, so $\xi(r)$ is independent of r and we have $\xi = k_d$, where k_d represents the chain dissociation kinetic rate.

3.2. Free energy of permanent network

Permanent network could demonstrate shape memory effects by changing water content (Zhang et al., 2014; Zhao et al., 2019). Most of the commonly used models do not involve W-SME in hydrogels (Chen et al., 2021; Hu et al., 2022). However, in Section 2, our experimental results suggest that T-SME and W-SME are coupled via the double networks. On the one hand, the structure of temporary network is inherited from the permanent network. On the other hand, the deformation of permanent network is influenced by the temporary network. The mechanism of W-SME of hydrogels is that glass transition temperature T_g changes with moisture. When the water content of SMHs is high, chain mobility is high due to a great deal of hydrogen bonds. As the water content decreases, hydrogen bonds are gradually broken, molecular chains become less mobile, and T_g increases. The effect of water content on T_g can be described by the Fox–Flory equation (Hiemenz and Lodge, 2007; Truong et al., 2011)

$$\frac{1}{T_g} = \frac{\phi}{T_d} + \frac{1-\phi}{T_w}, \tag{14}$$

where T_d represents the glass transition temperature for the dry network and T_w is the pure water transition temperature.

The permanent network can be considered as the simplification of the temporary network in the absence of attachment and detachment. To capture water-induced shape memory, using the network decomposition method, the permanent network is divided into two parts through the deformation condition and drying process. The part of the permanent network of which the reference configuration is the dried SMHs is denoted as Part 1. Part 2 refers to the networks transformed from Part 1 due to a decrease in the water content and its reference state is the state when drying begins. Consequently, Ψ_P is expressed as a unified form with Eq. (10), namely

$$\Psi_P(\mathbf{F}, c, T) = \underbrace{J\left[\langle\langle \gamma_{P1}(r, c, T)\psi(r)\rangle\rangle - \langle N_{P1}\psi(r_0)\rangle\right]}_{\text{Part 1}}$$
$$+ \underbrace{J\left[\langle\langle \gamma_{P2}(r, c, T)\psi(r)\rangle\rangle - \langle N_{P2}\psi(r_0)\rangle\right]}_{\text{Part 2}}, \tag{15}$$

where subscripts $P1, P2$ denote Part 1 and Part 2, respectively. N_{P1}, N_{P2} represent cross-linked chain number of the two Parts, respectively. The expression of N_{P2} is assumed as

$$N_{P2} = N_P e^{\eta\left(\frac{T_g - T_d}{T_g - T_w}\right)} \tag{16}$$

and $N_{P1} = N_P - N_{P2}$, where N_P is the number of cross-linked molecular chain per current volume for temporary network and η is a material parameter.

3.3. Thermodynamic framework

From Sections 3.1 and 3.2 and combining Eqs. (1), (2), (3), (10), (15), Ψ reads:

$$\Psi(\mathbf{F}, c, T) = J\left[\langle\langle \gamma_{P1}(r, c, T)\psi(r)\rangle\rangle - \langle N_{P1}\psi(r_0)\rangle\right]$$
$$+ J\left[\langle\langle \gamma_{P2}(r, c, T)\psi(r)\rangle\rangle - \langle N_{P2}\psi(r_0)\rangle\right]$$
$$+ J\left[\langle\langle \gamma(r, c, T)\psi(r)\rangle\rangle - \langle N\psi(r_0)\rangle\right]$$
$$+ \mu_0 c + RT\left[c\ln\frac{\Omega c}{1+\Omega c} + \frac{\chi c}{1+\Omega c}\right] + \frac{1}{2}K(J - (1+c\Omega))^2. \tag{17}$$

The evolution of the system must also satisfy the constraint deduced from the increase of entropy which leads to:

$$\dot{\Psi} + \eta_R \dot{T} - \frac{1}{2}\mathbf{T} : \dot{\mathbf{C}} - \mu \dot{c} + \frac{1}{T}\mathbf{q} \cdot \nabla T + \mathbf{j} \cdot \nabla \mu \leq 0, \tag{18}$$

where η_R denotes the entropy per unit volume, $\mathbf{T}$ is the second Piola–Kirchhoff stress, $\mathbf{C}$ represents the right Cauchy–Green tensor, $\mathbf{q}$ is the heat flux and $\mathbf{j}$ is the fluid flux (for definitions of all tensors, see Holzapfel, 2002). Substituting Eq. (17) into Eq. (18), the Cauchy stress σ, the conjugate work of the deformation rate is obtained as

$$\sigma = \frac{N_{P1}^R k_b T}{J}\left(\varsigma_{P1} - \mathbf{I}\right) + \frac{N_{P2}^R k_b T}{J}\left(\varsigma_{P2} - \mathbf{I}\right) + \frac{N_R k_b T}{J}\left(\varsigma - \mathbf{I}\right)$$
$$+ K\left(J - 1 - \Omega c\right)\mathbf{I}, \tag{19}$$

where the detailed proof is given in the supporting material S1, $N_{P1}^R = JN_{P1}$, $N_{P2}^R = JN_{P2}$ and $N_R = JN$, which represent the cross-linked chain per reference volume. Each term in Eq. (19) controls the different behavior of SMHs. The first and second terms associated with the permanent network produce the entropic elastic deformations and W-SME, respectively. The third term associated with the temporary network produces the T-SME and ς is called the chain distribution tensor (Vernerey et al., 2017). The last term is our approximation for the incompressible limit.

Considering that SMHs are in a steady state, namely $\dot{N} = 0$, we deduce an explicit evolution equation for the distribution tensor (the detailed demonstration is provided in the supporting material S2):

$$\varsigma = e^{-\bar{k}_d(T-T_0)}\mathbf{F}\,\mathbf{F}^{-1}(T_0)\,\mathbf{F}^{-T}(T_0)\mathbf{F}^T$$
$$+ \bar{k}_d \mathbf{F}\left(\int_{T_0}^{T} e^{-\bar{k}_d(T-\Lambda)}\mathbf{F}^{-1}(\Lambda)\mathbf{F}^{-T}(\Lambda)d\Lambda\right)\mathbf{F}^T, \tag{20}$$

where T_0 is the temperature above which dynamic bonds begin to associate, $\bar{k}_d$ is the rate of dissociation with temperature ($\bar{k}_d \dot{T} = k_d$) and $\mathbf{F}(T_0)$ is programming deformation gradient. The initial condition is then $\varsigma|_{T_0=0} = \mathbf{I}$ and $\bar{k}_d$ is assumed as a constant. Note that the permanent network can be considered as the simplification of the temporary network in the absence of attachment and detachment ($k_d = 0$). Eq. (20) simplifies as

$$\varsigma = \mathbf{F}\mathbf{F}^{-1}(T_0)\mathbf{F}^{-T}(T_0)\mathbf{F}^T, \tag{21}$$

which can be further written as $\varsigma_{P1} = \mathbf{F}\mathbf{F}^T$ and $\varsigma_{P2} = \tilde{\mathbf{F}}\tilde{\mathbf{F}}^T$ since $\mathbf{F}(T_0) = \mathbf{I}$ and $\mathbf{F}(T_0) = \mathbf{F}(\phi_0)$ for two parts of the permanent network, respectively. $\tilde{\mathbf{F}} = \mathbf{F}\mathbf{F}^{-1}(\phi_0)$ represents the deformation gradient associated with W-SME. As mentioned in Section 3.2, these results imply that the theories of T-SME and W-SME can be developed in a unified statistically-based thermodynamic framework and can be degenerated to the form in agreement with our early work (Hu et al., 2022). During the experiment, ϕ is a quantity easier to measure than c. Using $\phi^{-1} = 1 + \Omega c$ (Chester et al., 2015) for nearly incompressible hydrogels, we replace the independent variable ϕ in all functions with c in the following sections.

3.4. Kinetics of dynamic bonds association and dissociation

3.4.1. Temperature responsive reaction rate

The deformation tensor of temporary network is derived in Section 3.2 and in this section, $N(\phi,T)$ introduced first in Eq. (4) is ascertained. For convenience, we use the notation $N(\phi,T)$ instead of $N(c,T)$ as mentioned before. Three factors for $N(\phi,T)$: (1) volume expansion, (2) dynamic bond association, (3) dynamic bond dissociation, can be represented by

$$\frac{dN(\phi,T)}{dt} = -N(\phi,T)\,\mathrm{div}\mathbf{v} + k_a\left[N^t - N(\phi,T)\right] - k_d N(\phi,T), \tag{22}$$

where N^t is the total number of cross-linked chains in the current state and $\mathrm{div}\,\mathbf{v} = \dot{J}/J$. The last two terms of the right end of the above equation capture the change of $N(\phi,T)$ due to the dynamic

bond association and dissociation. Since the kinetics of association and dissociation of dynamic bonds are assumed to be in steady state, it implies that when T and ϕ change, $N(\phi,T)$ simultaneously reaches the equilibrium value corresponding to the new T and ϕ. Consequently, following Eq. (22), $N(\phi,T)$ is obtained as:

$$N(\phi,T) = \frac{k_a}{k_a + k_d}\,\frac{N_T}{J}, \tag{23}$$

where $N_T = J\,N^t$ is the total number of chains that can be cross-linked in the reference configuration. The equilibrium value of $N(\phi,T)$ is related to the ratio of k_a and k_d, also called forward and reverse reaction rates, respectively. The variation of k_a and k_d with temperature can be expressed by the Arrhenius equation (Sierra, 2012)

$$k_a(T) = k_{a0}\exp\left(-\frac{\Delta E_a}{k_b T}\right),$$
$$k_d(T) = k_{d0}\exp\left(-\frac{\Delta E_d}{k_b T}\right), \tag{24}$$

where k_{a0}, k_{b0} are frequency factors and ΔE_a, ΔE_d are the energy barriers for bond association and dissociation. $[k_a]^{-1}$ (respectively $[k_d]^{-1}$) represents the typical association constant (respectively the time dissociation constant) of the dynamic bonds (Stefani et al., 1997).

To be consistent with the material measurements in Section 2, we now take into account the hydrophobic effect as an example of study for the temperature responsive reaction rates. When the temperature is low, chains are assumed mostly free due to the weak hydrophobicity and MC remains transparent in the soluble state. In contrast, when the temperature is high, chains are cross-linked (as the transient network) due to strong hydrophobic interactions and MC in gel state becomes milky white. This process is called the sol–gel transition (Vyazovkin, 2016). To describe this phenomenon, the energy barriers ΔE_a and ΔE_d of Eq. (24) must be modified due to the temperature responsive activation energy namely:

$$\Delta E_a = \Delta \bar{E}_a + T\left(1 - \frac{T_{ref}}{T} - \ln\frac{T}{T_{ref}}\right)\Delta\bar{S},$$
$$\Delta E_d = \Delta \bar{E}_d - T\left(1 - \frac{T_{ref}}{T} - \ln\frac{T}{T_{ref}}\right)\Delta\bar{S}, \tag{25}$$

where $\Delta\bar{S}$, $\Delta\bar{E}_a$, $\Delta\bar{E}_d$ are thermodynamics parameters and T_{ref} is a reference temperature. The dependence of ΔE_d and ΔE_a as a function of the temperature T is illustrated in Fig. 7(a), and ΔE_a and ΔE_d vary in opposite ways. Indeed, at low temperature the bond association is difficult due to $\Delta E_a \gg \Delta E_d$ and the molecular chains are found in a free state. At high temperature, when $\Delta E_a \ll \Delta E_d$, molecular chains aggregate into networks.

Substituting Eq. (25) into Eq. (24), we obtain

$$k_a(T) = k_{a0}\exp\left(-\frac{\Delta\bar{E}_a + T\left(1 - \frac{T_{ref}}{T} - \ln\frac{T}{T_{ref}}\right)\Delta\bar{S}}{k_b T}\right),$$
$$k_d(T) = k_{d0}\exp\left(-\frac{\Delta\bar{E}_d - T\left(1 - \frac{T_{ref}}{T} - \ln\frac{T}{T_{ref}}\right)\Delta\bar{S}}{k_b T}\right). \tag{26}$$

Fig. 7(b) illustrates k_a, k_d and their ratio k_a/k_d as a function of temperature with some given parameters. According to Eq. (23), the variation of $N(\phi,T)$ with the temperature is determined by k_a/k_d. During the heating process, $\frac{k_a}{k_a+k_d}$ varies from 0 to 1 and MC transforms from sol state to gel state.

3.4.2. The role of water on chain cross-linking

As shown in Section 2.4.1, $N(\phi,T)$ first increases and then decreases with the variation of ϕ, which implies that there are new competing mechanisms concerning the role of the water content on $N(\phi,T)$.
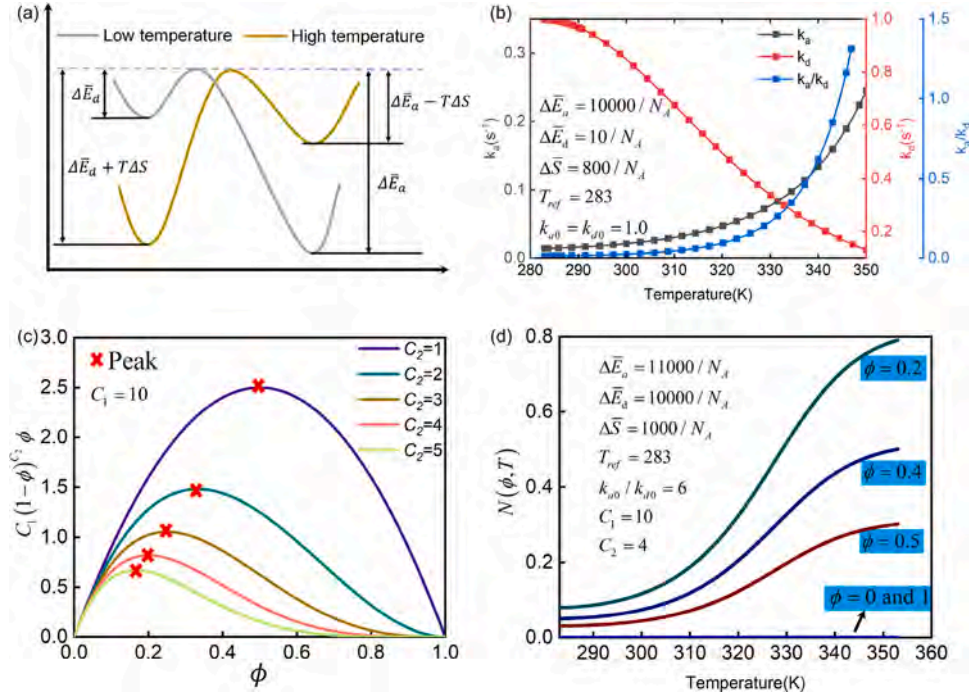
Fig. 7. (a) Schematic of the energy barriers ΔE_a and ΔE_d at low and high temperatures. (b) k_a, k_d and k_a/k_d as functions of temperature from Eq. (26), where parameters have been given arbitrary values. (c) $C_1(1 - \phi)^{C_2}\phi$ varies with ϕ under different C_2 exponents. (d) Following Eq. (27), $N(\phi, T)$ varies with temperature under different ϕ values.

This model considers two factors: the strength of the hydrophobic interaction and the number of molecular chains able to cross-link. The hydrophobic effect enhances with the increase of water also increasing the density of polymerized molecular chains, while free molecular chains per unit volume decreases with increasing water content. Hydrophobicity plays a major role at low water content, while the number of the free molecular chains per unit volume plays a major role at high water content. Therefore, there is a suitable water content that allows the maximum number of molecular chains to be polymerized.

This first factor was studied by Chen et al. (2009), where $N(\phi, T)$ varies monotonically with ϕ as $C_1(1 - \phi)^{C_2}$ where C_1, C_2 are fitting parameters. We now consider the contribution of the second factor on $N(\phi, T)$. We assume that each molecular chain can be cross-linked with all the others in the cross-linked region. Based on this hypothesis, we obtained that $N(\phi, T) \propto \phi$. Therefore, considering the above mechanisms and combining Eqs. (23) and (26), $N(\phi, T)$ is modified and reads:

$$N(\phi, T) = \frac{\frac{N_T}{J}C_1(1 - \phi)^{C_2}\phi}{1 + \frac{k_{d0}}{k_{a0}}\exp\left(-\frac{\Delta\bar{E}_d - \Delta\bar{E}_a - 2\left(T - T_{ref} - T\ln\frac{T}{T_{ref}}\right)\Delta\bar{S}}{k_bT}\right)} \quad (27)$$

Fig. 7(c) depicts the curves of $C_1(1 - \phi)^{C_2}\phi$, the part of $N(\phi, T)$ in Eq. (27), varying nonmonotonically with the polymer volume fraction ϕ, where there exists a peak value in each curve. As shown in Fig. 7(d), $N(\phi, T)$ is dependent on the temperature and the polymer volume fraction ϕ. Obviously, $N(\phi, T)$ increases monotonously with temperature, and first increases and then decreases with ϕ. Especially, when $\phi = 0$ or 1, $N(\phi, T) \equiv 0$.

3.5. Finite element implementation

We now give the main lines for the strategy of implementation in finite element algorithm. Our analysis is able to treat the initial water content after synthesis in SMHs as a free-swelling process. Then σ is modified as:

$$\sigma = \frac{G_I}{JJ_0}\left(J_0^{2/3}\mathbf{F}\mathbf{F}^T - \mathbf{I}\right) + \frac{\tilde{G}}{J}\left(\tilde{\mathbf{F}}\tilde{\mathbf{F}}^T - \mathbf{I}\right) + \frac{G_{II}}{J}\left(\varsigma - \mathbf{I}\right) + K\left(JJ_0 - \frac{1}{\phi}\right)\mathbf{I}, \quad (28)$$

where, $G_I, G_{II}, \tilde{G}$ which are respectively equal to $N_{P1}^R k_b T$ and $N_R k_b T/J_0$, $N_{P2}^R k_b T/J_0$, are named shear modulus of the permanent and temporary networks, respectively. The total gradient of the deformation results from : $\mathbf{F} = \mathbf{F}'\mathbf{F}_0$, where $\mathbf{F}_0 = \lambda_0\mathbf{I}$ represents the initial free swelling deformation, $J_0 = \det(\mathbf{F}_0)$ and $\mathbf{F}'$ denotes the deformation of SMHs after swelling. For convenience, $\mathbf{F}'$ will be denoted by $\mathbf{F}$ in the above equation and this change is also used below.

Equilibrium equations and boundary conditions thus are expressed as:

$$\begin{cases} \text{div}\sigma + \mathbf{b} = 0, & in \quad v, \\ \mathbf{u} = v, & on \quad a, \\ \sigma\mathbf{n} = \mathbf{t}, & on \quad a, \end{cases} \quad (29)$$

where $\mathbf{b}$ represents the body force in an arbitrary volumic region v, v is the displacement on the surface a, $\mathbf{u}$ denotes the displacement, $\mathbf{n}$ is unit vectors and $\mathbf{t}$ denotes the surface traction on a. The solution to the equation needs to satisfy the equilibrium equation and the boundary conditions, and the weak form of the above equation is used to solve the problem (Chester et al., 2015). Similar to Lin et al. (2020) and Mao et al. (2017), we treat SMH as a homogenous soft material and the distribution of water molecules is negligible.

The integral form corresponding to the above conditions is

$$\int_v \left(\sigma : \frac{\partial\mathbf{u}}{\partial\mathbf{x}}\right)dv = \int_a (\mathbf{u}\cdot\mathbf{t})\,da, \quad (30)$$

where we have ignored $\mathbf{b}$. The trial function $\mathbf{u}$ is discretized as

$$\mathbf{u} = \sum \mathbb{N}^\alpha\mathbf{u}^\alpha, \quad (31)$$

where α is the node number of a single element: $\alpha = 4$ for the plane strain element and 8 for the three dimensional element, used in this work.

Table 1
Selected parameters in constitutive model.

Notation	Variable	Value	Unit
λ_0	Initial stretch ratio	1.6087	–
T_0	Initial temperature	283	K
ϕ_0	Initial polymer volume fraction	0.24	–
G_I^T	Shear modulus of permanent network	12.80	kPa
G_{II}^T	Shear modulus of temporary network	42.68	kPa
K	Bulk modulus	1280	kPa
T_{ref}	Reference temperature	283	K
k_{d0}/k_{a0}	Fitting parameter	8.94	–
$\Delta \bar{E}_d - \Delta \bar{E}_a$	Fitting parameter	$-1000.45/N_A$	J
$\Delta \bar{S}$	Fitting parameter	$1148.3/N_A$	J/K
C_1	Fitting parameter	12.85	–
C_2	Fitting parameter	4.236	–
T_d	Glass transition temperature of dry network	452 (Chiantore et al., 1982)	K
T_w	Glass transition temperature of pure water	138 (Neamtu et al., 2006)	K
$\bar{k}_d$	Reaction rate	0.0001	K^{-1}
η	Parameter related to W-SME	0.2	–

Combining Eqs. (30) and (31), the unit residual is defined as

$$\left(\mathbf{R_u} \right)^\alpha = - \int_v \left(\sigma \frac{\partial \mathcal{N}^\alpha}{\partial \mathbf{x}} \right) dv + \int_a \left(\mathcal{N}^\alpha \mathbf{t} \right) da. \tag{32}$$

and the tangent lines: $-\partial \left(R_{u_i} \right)^\alpha / \partial u_k^\beta$ (see more details in Appendix A) are obtained by

$$\begin{aligned}
A_{ijkl} = &\frac{G_1}{JJ_0} \left(J_0^{2/3} \delta_{ik} F_{jm} F_{lm} + \delta_{jk}\delta_{il} \right) + \frac{\tilde{G}}{J} \left(\delta_{ik} \tilde{F}_{jb} \tilde{F}_{lb} + \delta_{jk}\delta_{il} \right) \\
&+ \frac{G_{II}}{J} \left(- \left(\varsigma_{il} - \delta_{il} \right) \delta_{jk} + \Xi_{iakn} \delta_{ja} F_{ln} \right) \\
&+ \frac{K}{\phi} \left((2JJ_0\phi - 1)\delta_{ji}\delta_{lk} - (JJ_0\phi - 1)\delta_{il}\delta_{jk} \right)
\end{aligned} \tag{33}$$

and we deduce:

$$\left(K_{u_i u_k} \right)^{\alpha\beta} = -\frac{\partial \left(R_{u_i} \right)^\alpha}{\partial u_k^\beta} = \int_v A_{ijkl} \frac{\partial \mathcal{N}^\alpha}{\partial x_j} \frac{\partial \mathcal{N}^\beta}{\partial x_l} dv - \int_a \mathcal{N}^\alpha \mathcal{N}^\beta \frac{\partial t_i}{\partial \mu_k} da. \tag{34}$$

3.6. Parameter identification

To demonstrate the consistency between the constitutive model and the thermo-aqueous behaviors of SMHs and to compare quantitatively the simulation results to the experimental ones, parameters specific to our samples are necessary. They are also extracted from experiments concerning the AAm-MC double network SMH (see more details in Appendix B). Hereafter a table present a list of the parameters required by our model and implemented in the simulations (see Table 1).

4. Results and discussions

The constitutive model is embedded into a UEL subroutine of ABAQUS software to reproduce the thermo-aqueous shape memory behaviors of SMHs under specific boundary conditions. Our aim is to compare the theoretical and numerical predictions with our experiments. Free swelling and isothermal uniaxial tension of SMHs are simulated and thermo-aqueous shape memory performance of our samples is investigated. Convergence analysis was carried out to guarantee that the simulation results is basically independent of the mesh.

4.1. Swelling results

To validate the validity of finite element simulation, we proposed a simulation example of SMHs free swelling by assumption that water
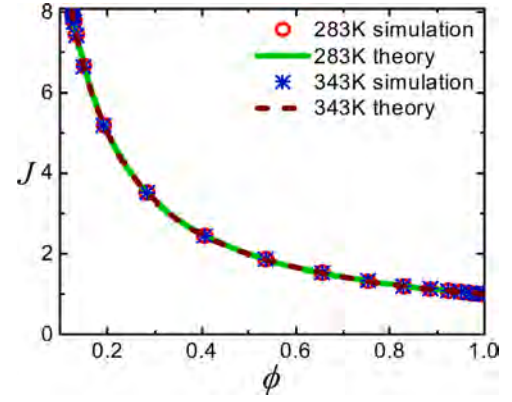

Fig. 8. Free swelling results at different temperatures.

diffusion has achieved a steady state. A cuboid with dimensions: 10 mm × 10 mm × 0.4 mm is divided into 400 three-dimensional elements with eight nodes and eight integral points and is modeled at different temperatures. For free swelling condition, the form of Eq. (28) can be simplified as

$$\sigma = \frac{G_I + G_{II}}{J} \left(J^{\frac{2}{3}} - 1 \right) \mathbf{I} + K \left(J - \frac{1}{\phi} \right) \mathbf{I}. \tag{35}$$

By considering boundary condition: $\sigma_{ij} = 0$, we can obtain curves between ϕ and J from Eq. (35) and finite element simulations. The simulation predications are in good agreement with the theoretical results in both 283 K and 343 K(Fig. 8).

4.2. Isothermal uniaxial tension

In uniaxial tension simulations as shown in Fig. 9(a), temperature were fixed at 283 K, 293 K, ..., 353 K and ϕ was fixed at concentration: 0.24, which was the same as in isothermal uniaxial tension tests. Two general cases, with plane strain (2D) and three dimensional (3D) configuration, were chosen with the geometric dimensions were 18 mm × 3 mm for 2D and 18 mm × 4 mm × 3 mm for 3D, respectively. Elements with four nodes and four integral points (2D elements) and elements with eight nodes and eight integral points (3D elements) were used, respectively. To match experimental boundary conditions, the left end was completely fixed, while the right end could only be deformed along the stretch direction. The displacement condition applied on the right end was 18 mm. Fig. 9(b) compares the results between simulations and experimental measurements at different temperatures. It is found that our model can capture isothermal uniaxial tension behaviors at different temperatures. As expected, the stress in the 3D case is less than that in the 2D case, in which the volume change can be only effective in two directions in the plane with a deformation constraint in the third direction.

4.3. Shape memory cycle simulation

4.3.1. Isoconcentration shape memory cycle simulations

A cuboid with dimensions given by 20 mm × 15 mm × 3 mm was adopted and 7200 (3D) elements were used. As same as the experimental set shown in Fig. 4(a), the specimen was firstly stretched from its initial length to 30 mm at 283 K. Then we maintained its length and rise the temperature from 283 K to a high temperature T_h. We also removed all constraints and made all boundaries traction-free in the next step. Finally, we decreased the temperature from T_h to 283 K in the last step. During the cycle, the water content was kept at its initial value. The two sides of the strip were completely fixed, except for the displacement along stretched direction at one side. Other surfaces
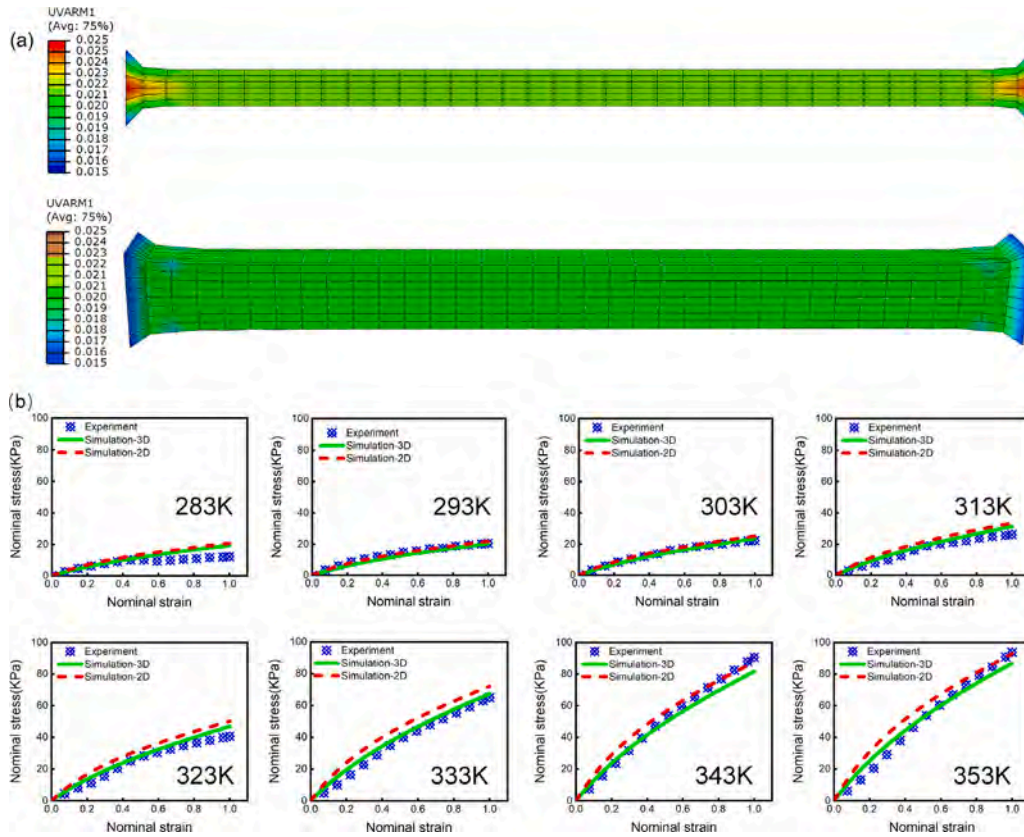
Fig. 9. Isothermal uniaxial tension results: (a) snapshots of SMHs after deformed under 2D and 3D cases (On left color codes representing the nominal stress component P_{11}), and (b) comparisons between experimental results and both 2D and 3D numerical predictions at different temperatures.

were traction-free. The shape memory behavior was represented by the normalized displacement u_{rn}.

An example of a shape memory process under $\phi = 0.24$ and $T_h = 343$ K is studied, and the u_{rn} from experiments and simulations at different temperatures are shown in Fig. 10(a). During stretching (step 1) and heating (step 2), simulations and experimental results are in full agreement, because the same u_{rn} value is predefined. Therefore, results in step 1 and step 2 are not emphasized in the following discussions. At the end of step 3, shape fixed ratios R_f are 71% from experimental records and 75% from simulated results which means that R_f can be captured by this model. In free recovery process (Step 4), u_{rn} decreases as temperature decreases. Although there are some differences between experimental and simulated results, our model captures the main trends of u_{rn}. At the end of step 4, R_c are 83% and 73% from experimental and simulated results, respectively. The possible reason for the difference between experimental and theoretical results is that the parameters utilized in shape memory process simulations are identified from the isothermal uniaxial tension and the isothermal uniaxial tension may not capture all properties of SMHs during shape memory cycle.

Shape memory behaviors of SMHs under different T_h and initial polymer volume fraction were studied, where three different temperatures 313 K, 328 K and 343 K and three different ϕ, namely 0.12, 0.17, 0.4, were adopted. The u_{rn} varying with T under different T_h are shown in Fig. 10(b). For each T_h, simulations and experimental results are consistent. Note that three simulated curves correspond to different R_f at the end of step 3, but coincide during step 4 because N is independent of the thermal history in our model. Experimental observations showing the similar trends and differences among the curves may be caused by experimental error. Fig. 10(c) shows u_{rn} as a function of T under various ϕ during step 3 and step 4. We can notice that all u_{rn} versus T curves obtained from experiments and simulations display approximately the same trends during step 4 and the values of u_{rn} versus T are dependent

on R_f. At the end of step 3, R_f initially increases and then reaches two similar values as decreasing polymer volume fraction, which means that R_f may do not vary monotonically with ϕ. As shown in Fig. B.1(b), the discrepancy between experimental and simulations may be caused by the inaccuracy prediction of the maximum value of R_f by the fitting function $C_1\phi(1 - \phi)^{C_2}$. To get a more comprehensive understanding of the influence of T and ϕ on R_f, other simulations with $T_h = 320$ K, 333 K and $\phi = 0.35$, 0.1 are added to Fig. 10(b) and (c), respectively. As indicated in Fig. 10(d), R_f monotonically increases with T_h, while R_f firstly increases and then decreases. Specifically, R_f varies 77.6% $\rightarrow$ 78.0% $\rightarrow$ 61.1% corresponding to ϕ varying 0.1 $\rightarrow$ 0.17 $\rightarrow$ 0.4, respectively.

The experiments demonstrate that the shape fixed ratio R_f is not a monotonic function of polymer volume fraction as our theoretical analysis which explains this behavior even if the agreement is only qualitative.

4.3.2. Thermo-aqueous shape memory simulations

Additive numerical simulations were implemented to capture thermo-aqueous coupled shape memory behaviors of SMHs. The geometric model, element type and dimensions were the same as in Section 4.3.1. Four simulations with various η values (0.1,0.2,0.3,0.4) were implemented and simulations for each η were compared with experimental results. As illustrated in Fig. 5(a), six steps were set up in these simulations following the same procedure as in experiments.

Fig. 11(a) shows the displacement contours of SMHs along the stretching direction during temperature-water content controlled shape memory cycle. SMHs keep their deformed shape rather than recover their initial shape during step 5, which indicates a quite different behavior compared with temperature-induced shape memory cycle, in which SMHs can recover their initial shape (shown in Section 4.3.1). The interpretation of this feature is that: as T_g increases due to the
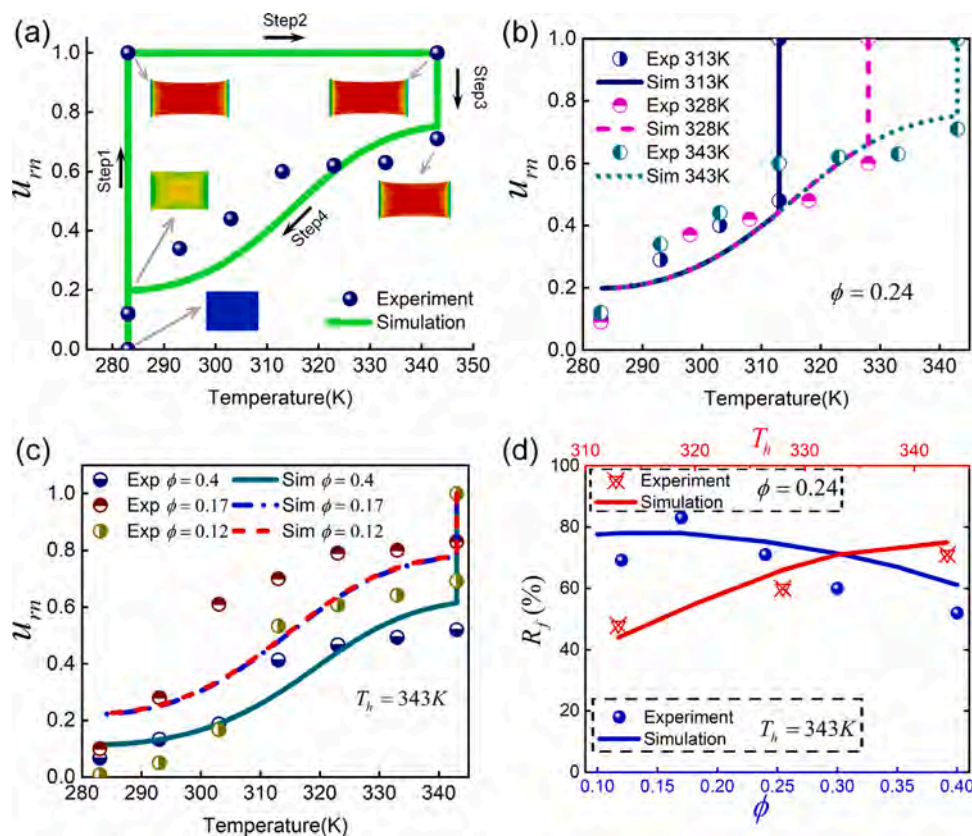
Fig. 10. Shape memory cycle results with constant water content: (a) normalized displacement as a function of temperature and snapshots of SMHs during the whole shape memory process from experimental and simulation results, (b) comparison between numerical predictions and experimental results at different fixed temperatures, (c) comparison between numerical predictions and experimental results with different polymer volume fraction, and (d) shape fixed ratio R_f as a function of ϕ from experimental observations and simulated results.

increase of ϕ during step 4, the chain mobility decreases and the programmed shape is maintained. There are two opposite effects on SMHs: the dissociation of dynamic bonds leads to the recovering of initial SMHs shape, namely T-SME, while the increase of T_g leads to the maintenance of the deformed shape, namely W-SME. During step 5, the effect of W-SME is dominant. During step 6, the chain mobility decreases due to the increase in water content, and the SMHs samples can go back to their initial configurations. It can be found that the shape memory behavior caused by temperature and water are coupled and our model can capture this key feature.

Fig. 11(b) shows the displacement u_r at the one end of SMHs varying with ϕ obtained from simulations and experimental results with various η from step 4 to step 6. All simulations can capture the trend of u_r varying with ϕ for each η. It can be seen that the simulations of u_r increase with η at fixed ϕ. A relatively better result is obtained when $\eta = 0.2$, which is used in the following simulations. There is a relatively large error when ϕ is greater than 0.4, which is probably attributed to the failure of visco-elasticity and the coupling of water molecule diffusion and nonlinearities due to large deformations taken into account in our model.

4.4. Discussion

Here a micro-macro constitutive model is developed to capture the thermo-aqueous behaviors for double network shape memory hydrogels with potentially dynamic bonds. This model considers the temperature-water responsive association or dissociation of dynamic bonds for the temporary network and for the permanent network water-induced chain mobility through the Fox–Flory equation. This theoretical model is embedded into a UEL subroutine of ABAQUS software to simulate the mechanical answer of SMHs and characteristic features have been

demonstrated as (1) the stiffness of SMHs increases with temperature, (2) the shape fixed ratio increase and then decrease with water content, (3) the thermo-aqueous coupling shape memory behavior. The representative mechanism of hydrophobic interaction is introduced into our theoretical model to investigate association and dissociation of dynamic bonds. Therefore, our model can be used for a wider range of material systems. It is worth noting that it does not consider the viscoelastic behavior of SMHs under low water content and the coupling of thermal-fluid transport-finite deformation. The differences between simulations and experimental results may result from these two limitations and these sophisticated and challenging issues will be investigated in the future.

One can conclude that T-SME can quickly fix the programmed shape of SMHs, but the maintenance of this shape will require the temperature to be controlled within a small range, which is uneasy. W-SME also can realize the shape programming of SMHs, however, a lot of time is required to remove the unwanted water. Furthermore, a low shape fixed ratio occurs due to the reduction of the water content. Therefore, the combination of the two stimuli allows for a rapidly fixing programmed shapes of SMHs and an extension of the effective temperature range to maintain temporary shapes.

The proposed constitutive model of SMHs may find potential applications ranging from the fabrication of micro-devices of sensors, actuators and functional components for biomedical and soft robotics (Shiblee et al., 2019; Zhan et al., 2018; Carrico et al., 2017). Traditional fabrication methods of soft matter device require mold design and are generally restricted to the fabrication of simple shapes. Recently, 4D printing of hydrogels was employed to fabricate hydrogel devices (Zhao et al., 2021; Zhang et al., 2019). However, printable responsive and active materials for soft sensors and actuators are inadequate (Shiblee
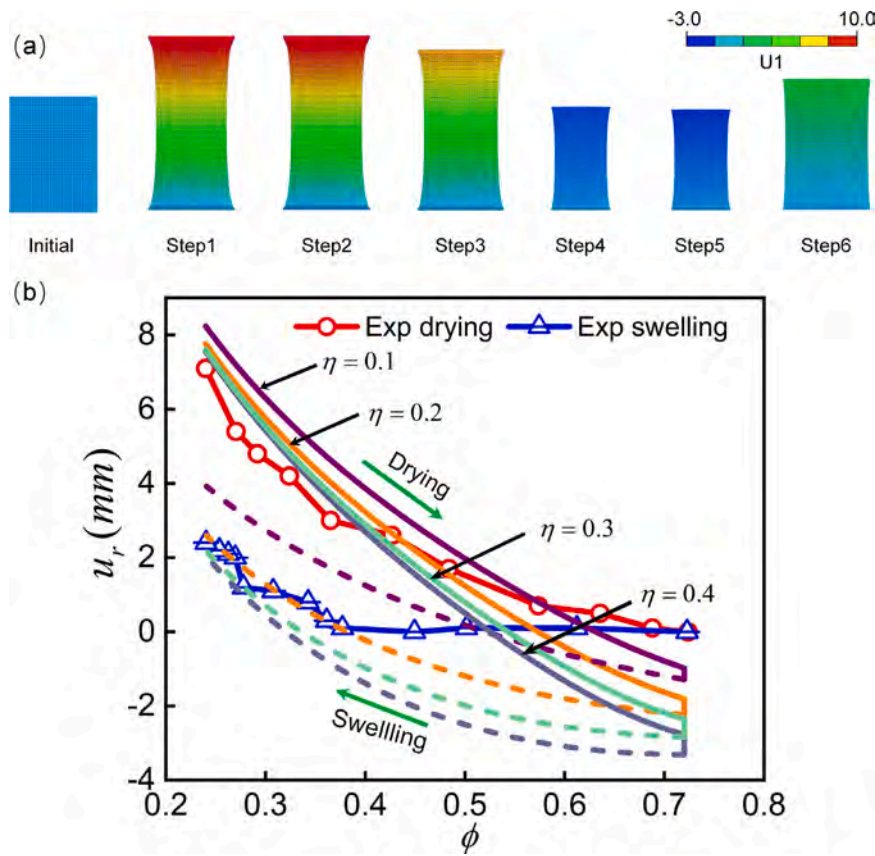
Fig. 11. (a) Contours of displacement U_1 of SMHs along the stretching direction during the shape memory cycle. (b) Displacement of one end of the strip as a function of ϕ, the water content decreases or increases during thermo-aqueous coupling shape memory cycle.
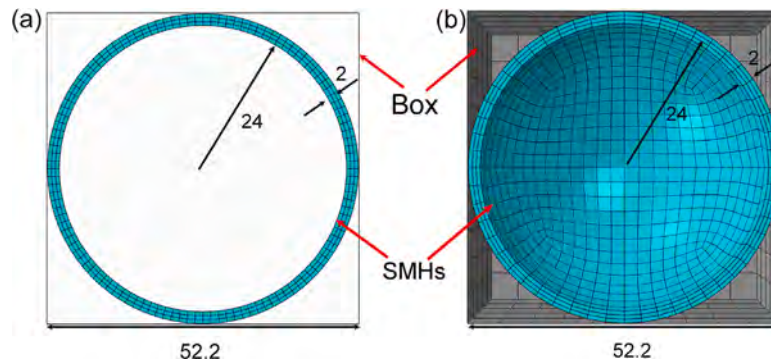

Fig. 12. Geometry and mesh of simulation models: (a) 360 2D elements for SMHs and R2D2 element for box under 2D case, and (b) 3276 3D elements for SMHs and R3D4 elements for box under 3D case (half of model).

et al., 2019). Our work may provide a convenient method for fabrication of soft sensors and actuators by using the temperature and water coupling SME of SMHs.

Two illustrative simulations to fabricate complex shapes by using temperature-water induced SME of SMHs are presented. The two-dimensional and three-dimensional geometry models of SMHs with their meshes are depicted in Fig. 12(a) and (b), respectively. External boxes are rigid bodies with fixed boundary conditions and surface-to-surface contact of frictionless property is set between the outer surface of SMHs and the inner surface of the box. The conditions of temperature and polymer volume fraction are applied sequentially in four steps, that

is,

$$\text{Temperature}(T): \quad 283\ \text{K} \rightarrow 283\ \text{K} \rightarrow 343\ \text{K}$$
$$\rightarrow 343\ \text{K} \rightarrow 283\ \text{K}$$

$$\text{Polymer volume fraction}(\phi): \quad 1.0 \quad \rightarrow 0.4 \quad \rightarrow 0.4 \quad \rightarrow 1.0 \quad \rightarrow 1.0$$

Fig. 13 illustrates the 2D and 3D displacement contours of SMHs under a specific constraint at initial time, end of step 2 and end of final step. Subjected to step 1, the water content of SMHs increases and SMHs with simple shape starts to swell, but due to the existence of the boundary constraints, the buckling occurs, which results in the complicated shape of SMHs. Then, through step 2, these complicated shape can be quickly maintained utilizing the T-SME of SMHs, however which needs the temperature to be kept in a small range. Third, the water content of SMHs is lowered, which can realize the maintenance
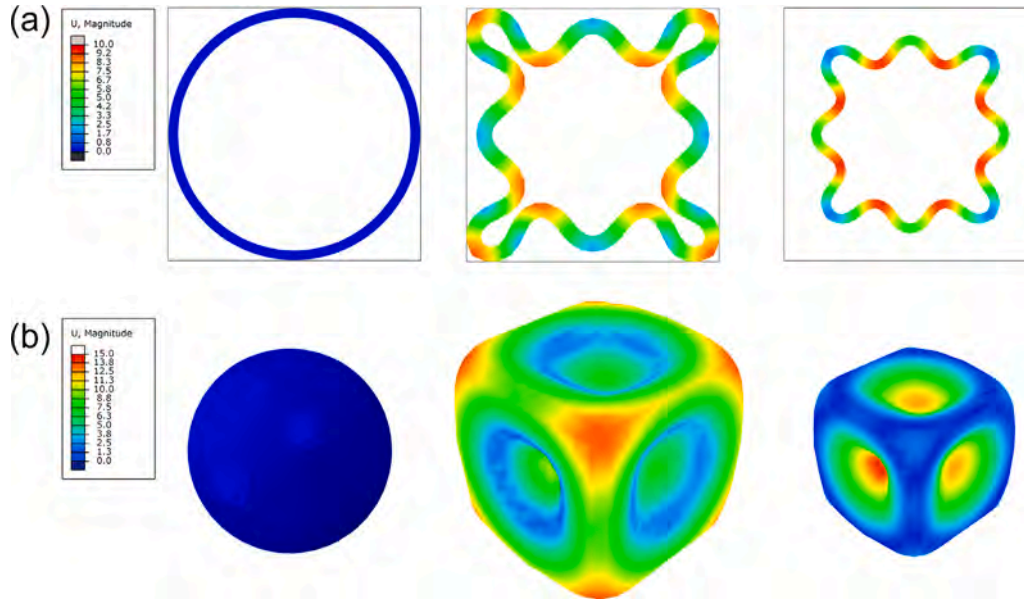
Fig. 13. The deformed configurations of SMHs at initial time, end of step 2 and end of final step: (a) 2D case and (b) 3D case.

of the complicated shape in a wide range of temperature, so finally the temperature can be recovered to room temperature and the desired shape is obtained permanently. It can be found that temperature and water content are the same in initial and final states and SMHs with simple shapes are deformed into complex shapes. Specifically, the circular SMHs are converted into a corrugated shape and the spherical SMHs are converted into a shape similar to a sieve. Note that traditional hydrogels do not have this capability given by elasticity. These results may provide new solutions for the fabrication of micro-devices with sophisticated configurations of sensors, actuators and functional components based on hydrogels.

5. Conclusions

In this work, thermo-aqueous coupling SME of double network SMHs is investigated. In conditional four-step shape memory cycles, the water contents of SMHs play a significant role in the shape fixed ratio, which first increases and then decreases with water content. This implies that a critical water content corresponding to the highest shape fixed ratio exists. To explore the coupling effect of temperature and water on SME of SMHs, a well-designed six-step experiment is conducted, where the key features of SMHs are identified. Based on experimental results and transient network theory, a micro-macro constitutive model is developed by utilizing temperature responsive energy barrier and water associated aggregation strength. The "hydration effect" and temperature-water responsive association and dissociation of dynamic bonds are involved in this theory, where additionally, the maximum value of water-associated polymerizable molecular chains per unit volume is proposed. As a validation, this theory is embedded into a user element subroutine of ABAQUS software to simulate the mechanical behavior of SMHs under isothermal uniaxial tension and shape memory cycles. The theoretical predictions and experimental results show good agreement. Based on SMHs thermo-aqueous shape memory effect investigated in this work, a new fabrication method for the of micro-devices of sensors, actuators and functional components is proposed and may be used in the field of biomedical and soft robotics.

Declaration of competing interest

The authors declare that they have no known competing financial interests or personal relationships that could have appeared to influence the work reported in this paper.

Data availability

Data will be made available on request.

Appendix A. Details of tangential stiffness matrix

In the present section, detailed derivations of tangential stiffness matrix $\left(K_{u_i u_k} \right)^{\alpha\beta}$ also called matrix AMATRX are listed. The form of tangential stiffness matrix is expressed as (Chester et al., 2015)

$$\left(K_{u_i u_k} \right)^{\alpha\beta} = -\frac{\partial \left(R_{u_i} \right)^{\alpha}}{\partial u_k^{\beta}} = \int_v \left(\frac{\partial \mathbb{N}^{\alpha}}{\partial x_j} \left(A_{ijkl} \right) \frac{\partial \mathbb{N}^{\beta}}{\partial x_l} \right) dv - \int_a \mathbb{N}^{\alpha} \mathbb{N}^{\beta} \frac{\partial t_i}{\partial \mu_k} da,$$

(A.1)

where $A_{ijkl} = J^{-1} F_{jm} F_{ln} (A_R)_{imkn}$. **A** and $\mathbf{A}_R$ are defined in current configuration and reference configuration, called spatial tangent modulus and referential tangent modulus, respectively. The first P-K stress $\mathbf{P} = J\boldsymbol{\sigma}\mathbf{F}^{-T}$ is defined to derive $\mathbf{A}_R$ and according to Eq. (28), **P** is obtained as

$$\mathbf{P} = \frac{G_1}{J_0} \left(J_0^{2/3}\mathbf{F} - \mathbf{F}^{-T} \right) + \tilde{G} \left(\tilde{\mathbf{F}}\tilde{\mathbf{F}}^T\mathbf{F}^{-T} - \mathbf{F}^{-T} \right)$$
$$+ G_{II} (\boldsymbol{\varsigma} - \mathbf{I}) \mathbf{F}^{-T} + K \left(J^2 J_0 - \frac{J}{\phi} \right) \mathbf{F}^{-T}.$$

(A.2)

Hence

$$\mathbf{A}_R = \frac{\partial \mathbf{P}}{\partial \mathbf{F}}$$
$$= \frac{G_1}{J_0} \left(J_0^{2/3}\frac{\partial \mathbf{F}}{\partial \mathbf{F}} - \frac{\partial \mathbf{F}^{-T}}{\partial \mathbf{F}} \right) + \tilde{G} \left(\frac{\partial \mathbf{F}}{\partial \mathbf{F}}\mathbf{F}^{-1}(\phi_0)\mathbf{F}^{-T}(\phi_0) - \frac{\partial \mathbf{F}^{-T}}{\partial \mathbf{F}} \right)$$
$$+ G_{II} \left((\boldsymbol{\varsigma} - \mathbf{I}) \frac{\partial \mathbf{F}^{-T}}{\partial \mathbf{F}} + \frac{\partial (\boldsymbol{\varsigma} - \mathbf{I})}{\partial \mathbf{F}}\mathbf{F}^{-T} \right) + K \left(2JJ_0 - \frac{1}{\phi} \right) \mathbf{F}^{-T} \otimes \frac{\partial J}{\partial \mathbf{F}}$$
$$+ K \left(J^2 J_0 - \frac{J}{\phi} \right) \frac{\partial \mathbf{F}^{-T}}{\partial \mathbf{F}}.$$
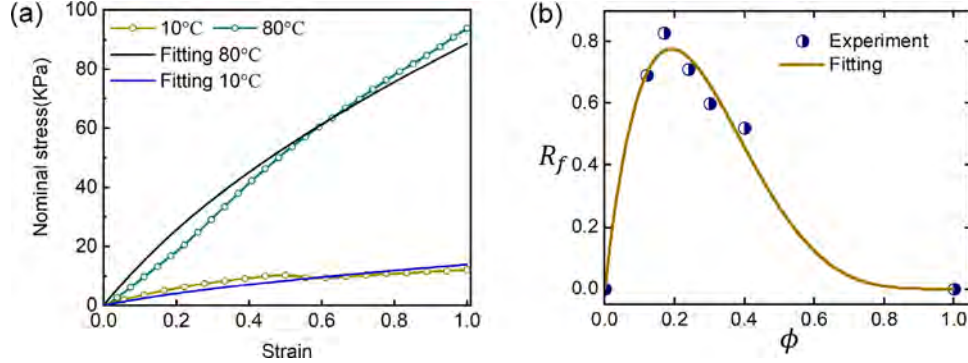
(A.3)

Fig. B.1. (a) Fitting results from uniaxial tension test at 10 °C and 80 °C. Fitting result of $C_1(1-\phi)^{C_2}$, where we assumed that R_f equals to zero for pure water and dry polymer network and two points (0,0) and (1,0) are added.

The component form is expressed as

$$
\begin{aligned}
\left(A_R\right)_{ijkl} = & \frac{G_1}{J_0}\left(J_0^{2/3}\delta_{ik}\delta_{jl}+F_{li}^{-1}F_{jk}^{-1}\right)+\tilde{G}\left(\delta_{ik}F_{lb}^{-1}(\phi_0)F_{jb}^{-1}(\phi_0)\right.\\
& \left.+F_{li}^{-1}F_{jk}^{-1}\right)\\
& +G_{II}\left(-\left(\varsigma_{im}-\delta_{im}\right)F_{lm}^{-1}F_{jk}^{-1}+\Xi_{imkl}F_{jm}^{-1}\right)\\
& +KJ\left(2JJ_0-\frac{1}{\phi}\right)F_{ji}^{-1}F_{lk}^{-1}-KJ\left(JJ_0-\frac{1}{\phi}\right)F_{li}^{-1}F_{jk}^{-1}.
\end{aligned}
\tag{A.4}
$$

In Eq. (A.4), $\Xi=\frac{\partial\varsigma}{\partial\mathbf{F}}$ and according to Eq. (20), its component form is derived as

$$
\begin{aligned}
\Xi_{imkl}= & \frac{\partial\varsigma_{im}}{\partial F_{kl}}\\
= & e^{-\bar{k}_d(T-T_0)}\frac{\partial F_{ia}}{\partial F_{kl}}F_{ab}^{-1}(T_0)F_{bc}^{-T}(T_0)F_{cm}^T\\
& +e^{-\bar{k}_d(T-T_0)}F_{ia}F_{ab}^{-1}(T_0)F_{bc}^{-T}(T_0)\frac{\partial F_{cm}^T}{\partial F_{kl}}\\
& +\frac{\partial F_{ia}}{\partial F_{kl}}\left[\int_{T_0}^T\bar{k}_dF_0^{-1}(\Lambda)F_0^{-T}(\Lambda)e^{-\bar{k}_d(T-\Lambda)}d\Lambda\right]_{ab}F_{bm}^T\\
& +F_{ia}\frac{\partial}{\partial F_{kl}}\left[\int_{T_0}^T\bar{k}_dF_0^{-1}(\Lambda)F_0^{-T}(\Lambda)e^{-\bar{k}_d(T-\Lambda)}d\Lambda\right]_{ab}F_{bm}^T\\
& +F_{ia}\left[\int_{T_0}^T\bar{k}_dF_0^{-1}(\Lambda)F_0^{-T}(\Lambda)e^{-\bar{k}_d(T-\Lambda)}d\Lambda\right]_{ab}\frac{\partial F_{bm}^T}{\partial F_{kl}}\\
= & e^{-\bar{k}_d(T-T_0)}\delta_{ik}\delta_{al}F_{ab}^{-1}(T_0)F_{bc}^{-T}(T_0)F_{cm}^T\\
& +e^{-\bar{k}_d(T-T_0)}F_{ia}F_{ab}^{-1}(T_0)F_{bc}^{-T}(T_0)\delta_{mk}\delta_{cl}+\delta_{ik}\delta_{al}(AA)_{ab}F_{bm}^T\\
& +\bar{k}_dF_{ia}F_{ac}^{-1}F_{cb}^{-T}\frac{\partial T}{\partial F_{kl}}F_{bm}^T+F_{ia}(AA)_{ab}\delta_{mk}\delta_{bl}\\
= & e^{-\bar{k}_d(T-T_0)}\delta_{ik}F_{lb}^{-1}(T_0)F_{bc}^{-T}(T_0)F_{cm}^T\\
& +e^{-\bar{k}_d(T-T_0)}F_{ia}F_{ab}^{-1}(T_0)F_{bl}^{-T}(T_0)\delta_{mk}+\delta_{ik}(AA)_{lb}F_{bm}^T\\
& +\bar{k}_d\delta_{im}\frac{\partial T}{\partial F_{kl}}+F_{ia}(AA)_{al}\delta_{mk},
\end{aligned}
\tag{A.5}
$$

where $(AA)_{ab}=\left[\int_{T_0}^T\bar{k}_d\mathbf{F}_0^{-1}(\Lambda)\mathbf{F}_0^{-T}(\Lambda)e^{-\bar{k}_d(T-\Lambda)}d\Lambda\right]_{ab}$. Moreover, the following well-known equations are used in derivation process of Eqs. (A.4) and (A.5)

$$
\begin{aligned}
&\frac{\partial F_{ij}}{\partial F_{kl}}=\delta_{ik}\delta_{jl}, && \frac{\partial F_{ij}^{-T}}{\partial F_{kl}}=-F_{li}^{-1}F_{jk}^{-1},\\
&\frac{\partial J}{\partial F_{ij}}=JF_{ij}^{-T}, && \frac{d}{dx}\int_{\psi(x)}^{\varphi(x)}f(\tau)d\tau=f[\varphi(x)]\varphi'(x)-f[\psi(x)]\psi'(x).
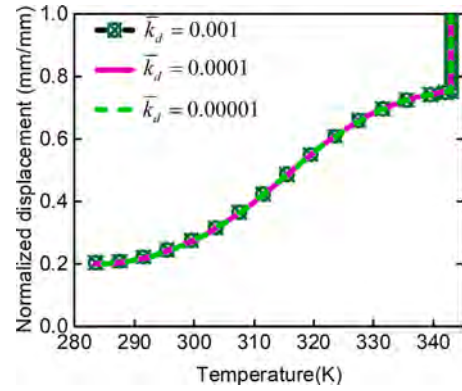\end{aligned}
\tag{A.6}
$$

Fig. B.2. The effect of $\bar{k}_d$ on SMHs during shape memory cycle.

Appendix B. Parameters determination

B.1. Parameter: ϕ_0, λ_0

The synthesized hydrogels intrinsically contains a certain content of water which results from the material fabrication process. It is assumed that the absorption of the water into the dried SMHs is a free-swelling process, that is $J_0=\lambda_0^3$ and $G_{II}=0,\tilde{G}=0$, so σ is expressed as:

$$
\sigma=\frac{G_1}{\lambda_0^3}\left(\lambda_0^2-1\right)+K\left(\lambda_0^3-\frac{1}{\phi_0}\right),
\tag{B.1}
$$

where $\phi_0=0.24$ according to our experiments, $\sigma=0$ and we take $K=100G_I$. By solving Eq. (B.1), we obtain $\lambda_0=1.6087$.

B.2. Parameters: T_0, G_I^T, G_{II}^T, T_{ref}, k_{d0}/k_{a0}, $\Delta\bar{E}_d-\Delta\bar{E}_a$, $\Delta\bar{S}$

These parameters can be determined through results of uniaxial tension texts. Two total shear modulus are defined $G_I^T=JJ_0N_Pk_bT$ and $G_{II}^T=JN_Pk_bT$ for permanent and temporary, respectively. In this condition, σ can be represented as

$$
\sigma=\frac{G_I}{\lambda_0}\left(\lambda^2-\frac{1}{\lambda}\right)+G_{II}\left(\lambda^2-\frac{1}{\lambda}\right),
\tag{B.2}
$$

where $\tilde{G}=0$ and $G_I=G_I^T$ are used. Since Methylcellulose is not gelation at $T_0=10$ °C (Li, 2002), we obtain that $G_{II}=0$ at this temperature. By fitting uniaxial tension results at 10 °C and 80 °C (Fig. B.1(a)), we obtained that $G_I^T=12.8$ kPa and $G_{II}^T=42.68$ kPa.

From previous section, we have $G_{II} = f(T)G_{II}^T$ and

$$f(T) = \cfrac{1}{1 + \cfrac{k_{d0}}{k_{a0}} \exp\left(-\cfrac{\Delta\bar{E}_d - \Delta\bar{E}_a - 2\left(T - T_{ref} - T\ln\frac{T}{T_{ref}}\right)\Delta\bar{S}}{k_b T}\right)}. \tag{B.3}$$

We take T_{ref} equal to initial programmed temperature, i.e. $T_{ref} = 283$ K. We choose 5 temperatures (293 K, 303 K, 333 K, 343 K, 353 K) to fit parameters and compare them with other temperatures, then we obtained that $k_{d0}/k_{a0} = 8.94$, $\Delta\bar{E}_d - \Delta\bar{E}_a = -1000.45/N_A$ and $\Delta S = 1148.3/N_A$, where N_A is Avogadro's constant.

B.3. Parameters C_1, C_2

Parameters C_1, C_2 fitted from data points of the variation of shape fixed ratio R_f vs. polymer volume fraction ϕ as shown in Fig. B.1(a). We assume that the maximum value of $C_1(1-\phi)^{C_2}\phi$ equal to 1, which means that all molecular are polymerized and we obtain that $C_1 = 12.85$ and $C_2 = 4.236$.

B.4. Parameters: η, $\bar{k}_d$

Parameters η associated with water-induced shape memory cycle cannot be determined directly by experiments listed in Section 2, where N_P can be determined but it is difficult to distinguish N_{P1} and N_{P2}. Simulations with different η during thermo-aqueous coupling shape memory cycle are discussed in Section 4.3.2. It is difficult to determine $\bar{k}_d$ from simple mechanical experiments introduced in Section 2 and we make $\bar{k}_d = 0.0001$ and simulations with various $\bar{k}_d$ was shown in Fig. B.2. It can be found the value of $\bar{k}_d$ has no effect on results within a certain range.

Appendix C. Supplementary data

Supplementary material related to this article can be found online at https://doi.org/10.1016/j.ijsolstr.2023.112395.

References

Annable, T., Buscall, R., Ettelaie, R., 1996. Network formation and its consequences for the physical behaviour of associating polymers in solution. Colloids Surf. A 112 (2), 97–116, A collection of Papers Presented at the Associating Polymers 1995 Meeting.

Ben Amar, M., Manyuhina, O., Napoli, G., 2011. Cell motility: a viscous fingering analysis of active gels. Eur. Phys. J. Plus 126, 1–15.

Bouklas, N., Landis, C.M., Huang, R., 2015. A nonlinear, transient finite element method for coupled solvent diffusion and large deformation of hydrogels. J. Mech. Phys. Solids 79, 21–43.

Carrico, J.D., Tyler, T., Leang, K.K., 2017. A comprehensive review of select smart polymeric and gel actuators for soft mechatronics and robotics applications: fundamentals, freeform fabrication, and motion control. Int. J. Smart Nano Mater. 8 (4), 144–213.

Chen, K., Baker, A.N., Vyazovkin, S., 2009. Concentration effect on temperature dependence of gelation rate in aqueous solutions of methylcellulose. Macromol. Chem. Phys. 210 (3–4), 211–216.

Chen, J., Huang, J., Hu, Y., 2020. 3D printing of biocompatible shape-memory double network hydrogels. ACS Appl. Mater. Interfaces 13 (11), 12726–12734.

Chen, Y., Zhang, H., Chen, J., Kang, G., Hu, Y., 2021. Hyperelastic model for polyacrylamide-gelatin double network shape-memory hydrogels. Acta Mech. Sinica 37 (5), 748–756.

Chester, S.A., Leo, C.V.D., Anand, L., 2015. A finite element implementation of a coupled diffusion-deformation theory for elastomeric gels. Int. J. Solids Struct. 52, 1–18.

Chiantore, O., Costa, L., Guaita, M., 1982. Glass temperatures of acrylamide polymers. Makromol. Chem. Rapid Commun. (Switzerland) 3 (5).

Curatolo, M., Lisi, F., Napoli, G., Nardinocchi, P., 2022. Circumferential buckling of a hydrogel tube emptying upon dehydration. arXiv preprint arXiv:2212.01240.

Curatolo, M., Nardinocchi, P., Teresi, L., 2021. Mechanics of active gel spheres under bulk contraction. Int. J. Mech. Sci. 193, 106147.

Dai, W., Guo, H., Gao, B., Ruan, M., Xu, L., Wu, J., Kirk, T.B., Xu, J., Ma, D., Xue, W., 2019. Double network shape memory hydrogels activated by near-infrared with high mechanical toughness, nontoxity, and 3D printability. Chem. Eng. J. 356, 934–949.

Fox, T.G., Flory, P.J., 1950. Second-order transition temperatures and related properties of polystyrene. I. Influence of molecular weight. J. Appl. Phys. 21 (6), 581–591.

Ge, Q., Chen, Z., Cheng, J., Zhang, B., Zhang, Y.-F., Li, H., He, X., Yuan, C., Liu, J., Magdassi, S., et al., 2021. 3D printing of highly stretchable hydrogel with diverse UV curable polymers. Sci. Adv. 7 (2), eaba4261.

Ge, Q., Luo, X., Iversen, C.B., Nejad, H.B., Mather, P.T., Dunn, M.L., Qi, H.J., 2014. A finite deformation thermomechanical constitutive model for triple shape polymeric composites based on dual thermal transitions. Int. J. Solids Struct. 51 (15–16), 2777–2790.

Ge, Q., Luo, X., Rodriguez, E.D., Zhang, X., Mather, P.T., Dunn, M.L., Qi, H.J., 2012. Thermomechanical behavior of shape memory elastomeric composites. J. Mech. Phys. Solids 60 (1), 67–83.

Hiemenz, P.C., Lodge, T.P., 2007. Polymer Chemistry. CRC Press.

Holzapfel, G.A., 2002. Nonlinear Solid Mechanics: A Continuum Approach for Engineering Science. Kluwer Academic Publishers, Dordrecht.

Hong, W., Zhao, X., Zhou, J., Suo, Z., 2008. A theory of coupled diffusion and large deformation in polymeric gels. J. Mech. Phys. Solids 56 (5), 1779–1793.

Hu, Y., Jia, F., Fu, i., Liu, Y., Leng, J., 2022. A constitutive model and its numerical implementation for reversible behavior of shape memory hydrogels. Smart Mater. Struct. 31 (9), 095032.

Hu, X., Zhang, D., Sheiko, S.S., 2018. Cooling-triggered shapeshifting hydrogels with multi-shape memory performance. Adv. Mater. 30 (26), 1707461.

Huggins, M.L., 1941. Solutions of long chain compounds. J. Chem. Phys. 9 (5), 440.

Li, L., 2002. Thermal gelation of methylcellulose in water: scaling and thermoreversibility. Macromolecules 35 (15), 5990–5998.

Li, Z., He, X., Cheng, J., Li, H., Zhang, Y.-F., Shi, X., Yu, K., Yang, H.Y., Ge, Q., 2021. Hydrogel-elastomer-based stretchable strain sensor fabricated by a simple projection lithography method. Int. J. Smart Nano Mater. 12 (3), 256–268.

Li, Z., Liu, Z., Ng, T.Y., Sharma, P., 2020. The effect of water content on the elastic modulus and fracture energy of hydrogel. Extreme Mech. Lett. 35, 100617.

Lin, J., Zheng, S.Y., Xiao, R., Yin, J., Wu, Z.L., Zheng, Q., Qian, J., 2020. Constitutive behaviors of tough physical hydrogels with dynamic metal-coordinated bonds. J. Mech. Phys. Solids 139, 103935.

Long, K.N., Dunn, M.L., Qi, H.J., 2010. Mechanics of soft active materials with phase evolution. Int. J. Plast. 26 (4), 603–616.

Lówenberg, C., Julich-Gruner, K.K., Neffe, A.T., Behl, M., Lendlein, A., 2020. Salt-induced shape-memory effect in gelatin-based hydrogels. Biomacromolecules 21 (6), 2024–2031.

Lu, W., Le, X., Zhang, J., Huang, Y., Chen, T., 2017. Supramolecular shape memory hydrogels: a new bridge between stimuli-responsive polymers and supramolecular chemistry. Chem. Soc. Rev. 46 (5), 1284–1294.

Luo, R., Wu, J., Dinh, N.-D., Chen, C.-H., 2015. Gradient porous elastic hydrogels with shape-memory property and anisotropic responses for programmable locomotion. Adv. Funct. Mater. 25 (47), 7272–7279.

Mahjoubi, H., Zaïri, F., Tourki, Z., 2019. A micro-macro constitutive model for strain-induced molecular ordering in biopolymers: application to polylactide over a wide range of temperatures. Int. J. Plast. 123, 38–55.

Maiti, B., Abramov, A., Franco, L., Puiggalí, J., Enshaei, H., Alemán, C., Díaz, D.D., 2020. Thermoresponsive shape-memory hydrogel actuators made by phototriggered click chemistry. Adv. Funct. Mater. 30 (24), 2001683.

Mao, Y., Chen, F., Hou, S., Qi, H.J., Yu, K., 2019. A viscoelastic model for hydrothermally activated malleable covalent network polymer and its application in shape memory analysis. J. Mech. Phys. Solids 127, 239–265.

Mao, Y., Lin, S., Zhao, X., Anand, L., 2017. A large deformation viscoelastic model for double-network hydrogels. J. Mech. Phys. Solids 100, 103–130.

Mistry, S.J., Govindjee, S., 2014. A micro-mechanically based continuum model for strain-induced crystallization in natural rubber. Int. J. Solids Struct. 51 (2), 530–539.

Neamtu, I., Chiriac, A., Nita, L., 2006. Characterization of poly(acrylamide) as temperature- sensitive hydrogel. J. Optoelectron. Adv. Mater. 8.

Osada, Y., Matsuda, A., 1995. Shape memory in hydrogels. Nature 376 (6537), 219.

Perera, M.M., Ayres, N., 2020. Dynamic covalent bonds in self-healing, shape memory, and controllable stiffness hydrogels. Polym. Chem. 11 (8), 1410–1423.

Qi, H.J., Nguyen, T.D., Castro, F., Yakacki, C.M., Shandas, R., 2008. Finite deformation thermo-mechanical behavior of thermally induced shape memory polymers. J. Mech. Phys. Solids 56 (5), 1730–1751.

Qu, S., 2022. 3D printing of hydrogel electronics. Nat. Electron. 1–2.

Shang, J., Le, X., Zhang, J., Chen, T., Theato, P., 2019. Trends in polymeric shape memory hydrogels and hydrogel actuators. Polym. Chem. 10 (9), 1036–1055.

Shiblee, M.N.I., Ahmed, K., Kawakami, M., Furukawa, H., 2019. 4D printing of shape-memory hydrogels for soft-robotic functions. Adv. Mater. Technol. 4 (8), 1900071.

Sierra, C.A., 2012. Temperature sensitivity of organic matter decomposition in the Arrhenius equation: some theoretical considerations. Biogeochemistry 108 (1), 1–15.

Stefani, G., Onofri, F., Valtorta, F., Vaccaro, P., Greengard, P., Benfenati, F., 1997. Kinetic analysis of the phosphorylation-dependent interactions of synapsin I with rat brain synaptic vesicles. J. Physiol. 504 (3), 501–515.

Tanaka, F., Edwards, S., 1992. Viscoelastic properties of physically crosslinked networks. 1. Transient network theory. Macromolecules 25 (5), 1516–1523.

Techawanitchai, P., Idota, N., Uto, K., Ebara, M., Aoyagi, T., 2012. A smart hydrogel-based time bomb triggers drug release mediated by pH-jump reaction. Sci. Technol. Adv. Mater..

Truong, M.Y., Dutta, N.K., Choudhury, N.R., Kim, M., Elvin, C.M., Nairn, K.M., Hill, A.J., 2011. The effect of hydration on molecular chain mobility and the viscoelastic behavior of resilin-mimetic protein-based hydrogels. Biomaterials 32 (33), 8462–8473.

Vernerey, F.J., Long, R., Brighenti, R., 2017. A statistically-based continuum theory for polymers with transient networks. J. Mech. Phys. Solids 107, 1–20.

Vyazovkin, S., 2016. A time to search: finding the meaning of variable activation energy. Phys. Chem. Chem. Phys. 18 (28), 18643–18656.

Wall, F.T., Flory, P.J., 1951. Statistical thermodynamics of rubber elasticity. J. Chem. Phys. 19 (12), 1435–1439.

Xiao, R., Mai, T.-T., Urayama, K., Gong, J.P., Qu, S., 2021. Micromechanical modeling of the multi-axial deformation behavior in double network hydrogels. Int. J. Plast. 137, 102901.

Xiao, R., Nguyen, T.D., 2013. Modeling the solvent-induced shape-memory behavior of glassy polymers. Soft Matter 9 (39), 9455–9464.

Xu, C., Tang, Q., Yang, H., Peng, K., Zhang, X., 2018. High-strength, thermally activated shape memory hydrogels based on hydrogen bonding between MAAc and NVP. Macromol. Chem. Phys. 1700636.

Zhan, Y., Gao, H., Wang, H., Xu, Z., Chen, X., Liu, B., Shi, Y., Lu, Y., Wen, L., Li, Y., 2018. Radiopaque highly stiff and tough shape memory hydrogel microcoils for permanent embolization of arteries. Adv. Funct. Mater. 28 (9), 1705962.

Zhang, Z., Demir, K.G., Gu, G.X., 2019. Developments in 4D-printing: a review on current smart materials, technologies, and applications. Int. J. Smart Nano Mater. 10 (3), 205–224.

Zhang, Y., Gao, H., Wang, H., Xu, Z., Chen, X., Liu, B., Shi, Y., Lu, Y., Wen, L., Li, Y., et al., 2018. Radiopaque highly stiff and tough shape memory hydrogel microcoils for permanent embolization of arteries. Adv. Funct. Mater. 28 (9), 1705962.

Zhang, J.L., Huang, W.M., Gao, G., Fu, J., Zhou, Y., Salvekar, A.V., Venkatraman, S.S., Wong, Y.S., Tay, K.H., Birch, W.R., 2014. Shape memory/change effect in a double network nanocomposite tough hydrogel. Eur. Polym. J. 58, 41–51.

Zhao, H., Huang, Y., Lv, F., Liu, L., Gu, Q., Wang, S., 2021. Biomimetic 4D-printed breathing hydrogel actuators by nanothylakoid and thermoresponsive polymer networks. Adv. Funct. Mater..

Zhao, W., Xu, H., Liu, Y., Xu, J., Luan, R., Feng, X., 2019. Temperature-dependent transmittance nanocomposite hydrogel with high mechanical strength and controllable swelling memory behavior. Eur. Polym. J. 112, 328–333.